K

NATIONAL AERONAUTICS AND SPACE ADMINISTRATION

TECHNICAL MEMORANDUM X-682

HEAT-TRANSFER AND PRESSURE DISTRIBUTIONS AT A

MACH NUMBER OF 6 FOR 70° SWEPT SLAB WINGS

WITH SHARP AND SPHERICAL NOSES AND

CYLINDRICAL LEADING EDGES*

By Robert A. Jones and Robert L. Trimpi

SUMMARY

Local heat-transfer coefficients and surface pressures in the region of the cylindrical leading edge of 70° swept delta wings with sharp and spherical noses were determined from wind-tunnel tests at a Mach number of 6; free-stream Reynolds numbers, based on leading-edge diameter, of 3×10^4, 6×10^4, and 23×10^4; and angles of attack from 0° to 30°. Within the range of 3 to 6 leading-edge diameters from the nose at angles of attack to 20°, the heat transfer to the leading edge of the sharp-nose wing was found to agree with values predicted by an easily applied theory. At angles of attack of 25° and 30°, the high Reynolds number data for the windward side of the leading edge indicate transitional or turbulent flow with measured heating rates much higher than theoretical values. Within the range of 2 to 5 leading-edge diameters from the nose, the heat transfer to the leading edge of the spherical-nose wing was found to be slightly higher than for the sharp-nose wing with higher heating rates for locations nearer the nose. In addition, the heat-transfer-coefficient ratios were found to be higher for the low Reynolds number data for locations near the nose than for the high Reynolds number data.

INTRODUCTION

The design of many proposed lifting-reentry configurations having delta-planform wings with blunt leading edges is hindered by the lack of data on the aerodynamic heating they will experience in the earth's atmosphere. Some theoretical and experimental studies of aerodynamic

heating at high Mach numbers have been made for wings, leading edges, and noses. For example, a theory was developed in reference 1 for predicting the rate of heat transfer to blunt-nose bodies at hypersonic speeds and in reference 2 for predicting heat transfer to bodies with yaw and large pressure gradients at hypersonic speeds. An experimental study of heat transfer to yawed cylinders at a Mach number of 4.15 is reported in reference 3, and other experimental studies of aerodynamic heating to delta wings at high Mach numbers are reported in references 4 to 8. Most of the data in these references were taken on wing surfaces at relatively large distances from the nose.

This report is concerned with detailed measurements of the aerodynamic heating to the blunt leading edge of slab delta wings in the vicinity of 2 to 6 leading-edge diameters from the nose and the effect of nose bluntness on the heating to the leading edge. The data of this paper were obtained as part of a general hypersonic wing study conducted at Langley Research Center in 1958 and 1959 and have been used internally in support of various programs. These data are being published at this time both to add to the general body of hypersonic-wing data and to present arguments for the evaluation of the surface entropy of sharp- and blunt-nose wings.

L
1
4
5
2

SYMBOLS

C_p	pressure coefficient
$C_{p,max}$	maximum pressure coefficient
c	specific heat
d	leading-edge diameter
h	local heat-transfer coefficient
$h_{\Lambda=0}$	theoretical laminar heat-transfer coefficient at the stagnation line of an unswept circular cylinder
l	distance from nose-leading-edge tangent point measured parallel to leading edge
M_∞	free-stream Mach number
p	local pressure

p_{sl} swept cylinder stagnation-line pressure

$p_{t,\infty}$ free-stream stagnation pressure

$p_{t,\sigma}$ stagnation pressure behind normal shock at free-stream Mach number

p_{∞} free-stream static pressure

q heat-transfer rate

R_d free-stream Reynolds number based on model leading-edge diameter

r radius of cylindrical leading edge

s distance along surface normal to leading edge measured from point of symmetry of leading edge

T_r recovery temperature

T_w surface temperature

t time

x distance from nose of blunt configuration along model center line

y distance along surface normal to the leading edge measured from point of tangency

α angle of attack

γ ratio of specific heat at constant pressure to the specific heat at constant volume taken to be 1.40

δ flow-deflection angle

ϵ_e angle between leading edge and free-stream direction

η acute angle between component of free stream normal to leading edge and plane of wing

$\theta \approx s/r$

$\theta_{eff} = \left| \eta + \theta \right|$

Λ_{eff} effective sweep, $90^{\circ} - \epsilon_e$

ρ density

τ thickness

MODELS

Two models having 70° swept cylindrical leading edges were tested. One was a semispan wing with a sharp nose and the other was a 3/4-span wing with a spherical nose. Sketches of the models are shown in figures 1 to 3 and photographs of the pressure models are shown in figure 4. The instrumented sections of the two models were interchangeable. For the sharp-nose configuration, the instrumented section of the model shown in figure 1 was mounted on a sharp flat plate as shown in figure 2. The leading-edge thickness of the plate was approximately 0.001 inch. For the spherical-nose configuration, the instrumented section was mounted to a blunt-nose wing section as shown in figure 3.

A small wing fence was located at the tip of each wing. This fence contained five holes which had a total area of approximately 40 percent of the effective area of the fence. This wing fence was used in an attempt to simulate the flow of an infinitely long wing by a wing of finite length.

The thermocouple locations are shown in figure 1. The thermocouples were made from number 30 iron-constantan wire and were spot welded to the inner surface of the skin. The skin was made of 0.030-inch-thick number 347 stainless steel. There was a total of 49 thermocouples wired to seven connecting plugs with seven thermocouples to each plug. However, the reference junction would handle only six connecting plugs or 42 thermocouples and therefore one connecting plug and its seven thermocouples were omitted from each series of tests. For most of the tests of the sharp-nose configuration, the thermocouples of station A were omitted; and for the blunt-nose configuration, the thermocouples at the leading edge of station E were generally omitted.

Pressure orifice locations are shown in figure 3. These orifices had a diameter of 0.040 inch and were connected by tubing to a mercury manometer.

TUNNEL, TEST TECHNIQUE, AND DATA REDUCTION

Tests were conducted in the Mach number 6.2 blowdown tunnel at the Langley Research Center. A complete description of this tunnel as well as a description of the test technique, data recording, and data reduction is given in reference 5; therefore, only a brief description is given herein.

Heat-transfer data were obtained by using a transient testing technique. The tunnel was started and brought to the desired operating conditions and then the model was rapidly injected into the airstream by a pneumatic piston which was located in a sealed box directly over the test section. The total time required for injection was about 0.25 second, but it is estimated that from the time the model first entered the airstream until steady flow was established was only 0.05 second. The model remained in the airstream for 3 to 10 seconds. Between runs the model was cooled by high-pressure air jets to room temperature.

Thermocouple outputs were recorded on magnetic tape by a Beckman 210 high-speed analog to digital data recording system at a rate of 40 times per second. Heat-transfer coefficients were obtained by fitting a second-degree curve to the data by the method of least squares and computing the time derivative of temperature on a card programed computer. The heat-transfer coefficient is given by the equation

$$ h = \frac{\rho c_T \frac{\partial T_w}{\partial t}}{T_r - T_w} \tag{1} $$

The method of obtaining recovery temperature T_r is discussed in the section of this report entitled "Results and Discussion."

Heat-transfer data were obtained at stagnation pressures from 20 to 165 lb/sq in. abs with stagnation temperatures varying from 300° to 450° F depending on the pressure. Pressure data were obtained only at stagnation pressures of 500 lb/sq in. abs because long running times and high pressure levels were required for the manometer to settle out. For the pressure tests, the stagnation temperature was approximately 500° F.

RESULTS AND DISCUSSION

Flow Pattern

Schlieren photographs of the flow are presented in figures 5 and 6 for the sharp- and spherical-nose models, respectively. In figure 5, the disturbance from the leading edge of the plate hits the leading edge of the wing very near to station A. (See figs. 1 and 3 for location of station A.) For this configuration, no heat-transfer or pressure data were taken at station A. The angle of inclination of the disturbance from the leading edge of the plate is near the free-stream Mach angle, and this disturbance causes no deflection of the wing leading-edge shock wave. Therefore, it is thought that the disturbance from the plate leading edge is very weak in comparison to the leading-edge shock wave of the wing. Note that the wing shock wave is curved and that it never becomes parallel to the leading edge. An increase in the angle of attack increases the distance between this shock wave and the leading edge.

From figure 6 it can be seen that part of the spherical-nose model between station E and the wing end plate is located in a region of a tunnel disturbance. The flow deflection across this disturbance was determined by pressure measurements made on a wedge and found to have a maximum of approximately $3/4^o$. For this configuration heat-transfer data were taken at stations A to D and at those thermocouples of station E for which s/r was greater than 2.5. (See figs. 1 and 3 for location of these stations.) Pressure data were taken at stations B to E and along the center line of the model. The effect of the tunnel disturbance on the data is discussed subsequently.

Note that the leading-edge shock wave is more nearly parallel to the leading edge for this configuration than for the sharp-nose configuration. The angle of attack has little effect on the shock-wave shape in the vicinity of the nose for the range of angles tested in this investigation; however, in the vicinity of the wing end plate, the distance between the shock wave and leading edge is increased with angle of attack in a manner similar to that of the sharp-nose configuration.

Pressure Distributions

Pressure-distribution data are presented first because they are used in the theoretical calculation of recovery temperatures and heat-transfer distributions. The data are plotted in figures 7 and 8 as the ratio $p/p_{t,\sigma}$ where p is the measured local pressure and $p_{t,\sigma}$ is the stagnation pressure behind a normal shock at the free-stream Mach

number. Also shown in figures 7 and 8 are the curves computed from modified Newtonian theory which predicts the distribution

$$\frac{c_p}{c_{p,max}} = \sin^2\delta \tag{2}$$

where δ is the deflection angle of the component of flow normal to the swept leading edge. This equation can be rewritten as

$$\frac{p}{p_{sl}} = \cos^2\theta_{eff} + \frac{p_\infty}{p_{sl}} \sin^2\theta_{eff} \tag{3}$$

where θ_{eff} is the complement of the deflection angle in the crossflow plane and p_{sl} is the stagnation line pressure of the cylindrical leading edge computed from oblique shock theory as

$$\frac{p_{sl}}{p_{t,\infty}} = \left(\frac{2\gamma}{\gamma+1} M_\infty^2 \cos^2\Lambda_{eff} - \frac{\gamma-1}{\gamma+1}\right)^{\frac{-1}{\gamma-1}} \left(\frac{\frac{\gamma+1}{2} M_\infty^2 \cos^2\Lambda_{eff}}{1 + \frac{\gamma-1}{2} M_\infty^2}\right)^{\frac{\gamma}{\gamma-1}} \tag{4}$$

Pressure distributions of the sharp-nose configuration are shown in figure 7. The theory predicts the pressure on that part of the cylindrical leading edge where $s/r < 1$ with reasonable accuracy at all angles of attack. At angles of attack less than 10° the theory predicts the pressure over the entire wing with reasonable accuracy, but for higher angles of attack and $s/r > 1$ the measured pressure is generally higher than theory. There is also a variation in pressure with distance from the nose. Station B is located approximately 3 leading-edge diameters from the nose; station C is approximately 4 diameters from the nose; and so forth. The pressure at station B is about 10 percent higher than theory in the region near the stagnation line. As the distance from the nose (l/d) increases, the measured pressure in this region approaches the theoretical pressure and becomes equal to it at station D or approximately 5 diameters from the nose.

Pressure distributions of the spherical-nose configuration are presented in figure 8. As was mentioned previously, station E of this configuration was located in the region of a tunnel disturbance. In figure 8(a) the pressure at station E is considerably higher than the

other data. The data taken with the model located in this tunnel posi-
tion are shown here since all of the heat-transfer data of the blunt-nose
configuration were taken in this same tunnel location. (However, no
heat-transfer data were taken at station E for $s/r < 1$.) As a check,
pressure data were taken (along the stagnation line at zero angle of
attack) with the model located in the tunnel such that this disturbance
did not hit the model. In this case the pressure at station E was the
same as the stations C and D data of figure 8(a). It is, therefore,
thought that this tunnel disturbance has very little effect on the data
of stations other than station E and that the station E data of the
spherical-nose configuration can be disregarded. The data of stations B,
C, and D are as much as 20 percent higher than the theoretical data in
the vicinity of the stagnation line. The variation of pressure with
distance from the leading edge (s/r) is different from that for the
sharp-nose configuration shown in figure 7. At angles of attack of 0°
and 5° the pressure is lower at station B (3 leading-edge diameters from
the nose), but for angles of attack above 10°, the trend is reversed and
the pressure is higher nearer the nose. In the neighborhood of the stag-
nation line, the measured pressure at all stations is always higher than
the theoretical pressure. The effect of the blunt nose is apparently
felt over the entire leading edge. The variation of pressure along the
center line of the model is plotted in figure 9. At angles of attack of
0° and 5° the pressure was slightly higher near the nose, at 10° it was
almost constant, and at higher angles of attack the pressure was higher
toward the trailing edge of the wing.

Heat-Transfer Distributions

Heat-transfer data are plotted in figures 10 and 11 as the ratio
$h/h_{\Lambda=0}$ where h is the local heat-transfer coefficient for laminar
flow and $h_{\Lambda=0}$ is the theoretical laminar heat-transfer coefficient
for the stagnation line of an unswept circular cylinder at the same
free-stream conditions. In order to determine local heat-transfer coef-
ficients from the measured heat-transfer rates, a laminar recovery factor
of 0.85 was assumed and a local recovery temperature was calculated.
The temperature potential was then the computed local recovery tempera-
ture minus the measured local wall temperature. The local recovery temp-
erature was computed differently for the two configurations. For the
sharp-nose configuration, T_r was calculated by assuming first that
the flow passed through a shock wave which was swept parallel to the
leading edge of the wing and that the flow was then expanded isentrop-
ically to the modified Newtonian pressure which is plotted in figures 7
and 8. For the spherical-nose configuration, T_r was calculated by
first assuming that the flow passed through a shock wave which was normal
to the free-stream flow direction and was then expanded to the modified

Newtonian pressure. The theoretical heat-transfer coefficient $h_{\Lambda=0}$ was taken from reference 9.

Also plotted in figures 10 and 11 are curves representing a theoretical laminar heat-transfer-coefficient distribution. The equation used to calculate this coefficient is

$$\frac{h}{h_{\Lambda=0}} = \cos \Lambda_{eff} \frac{q}{q_{\theta_{eff}=0}} \frac{\left(T_r - T_w\right)_{\theta_{eff}=0}}{\left(T_r - T_w\right)} \tag{5}$$

where the ratio $q/q_{\theta_{eff}=0}$ was obtained from the method of Lees (ref. 1) by using the pressure distribution predicted by modified Newtonian theory. For the case of negative values of s/r, the theoretical heat-transfer distribution was not computed for values of θ_{eff} larger than 90°.

Heat-transfer distributions of the sharp-nose configuration are presented in figure 10 for angles of attack from 0° to 30°. For this configuration, data were taken at stations B, C, D, and E at three Reynolds numbers. Note that data of figures 10(b), 10(c), and 10(d) cover a range of s/r from -4.4 to 4.4. In order to obtain data for values of s/r less than -0.3, runs were made with the model at negative angles of attack. To distinguish between these data, the flags and tails on the symbols denoting Reynolds number are on the right for data obtained at positive angles of attack and on the left for data obtained at negative angles of attack. The high Reynolds number data for an angle of attack of 10° and positive s/r have been omitted from figure 10(c). As a result of instrumentation difficulties these data appeared to be invalid.

Most of the data in the region near the stagnation line indicate that the flow is laminar. The exceptions to this are the data of figures 10(f) and 10(g) for which the angles of attack were 25° and 30°, respectively. At these angles of attack the flow pattern over the wing has changed such that the flow may be in a direction outward toward the leading edge. There is a general discussion of flow patterns over wings of this shape in references 6 and 8. Thus, the leading edge no longer behaves like a swept cylinder and the theory may be inapplicable. The variation of heat transfer with Reynolds number does, however, indicate the possibility of transitional or turbulent flow.

For angles of attack less than 20° there is no general trend in the variation of heat transfer with distance from the nose in these data which cover a range of approximately 3 to 6 leading-edge diameters from

the nose. This result indicates that the flow over this portion of the leading edge does approach that of an infinitely long wing. In order to obtain some information on the effect of the small wing fence which was located at the tip of the wing, the holes in the fence were closed and data were taken at zero angle of attack and at an angle of attack of 20°. These data showed no effect of closing the holes except in the immediate vicinity of the fence at an angle of attack of 20° where the heating was increased somewhat.

The heat-transfer distribution predicted by the theory shows reasonably good agreement with the data in the region near the stagnation line for angles of attack of 20° and less. On the slab portion of the wing $(s/r > 1.6)$, the measured data show poor agreement with the theoretical data, especially at the high angles of attack. The greater part of these measured data are for conditions of transitional flow as seen by the increase in heat-transfer coefficient with an increase in Reynolds number in figures 10(a) to 10(f).

The heat-transfer distributions of the spherical-nose configuration are presented in figure 11 for angles of attack from 0° to 20°. For this configuration, data were taken at stations A, B, C, D, and that portion of station E for which s/r is greater than 2.5. As was mentioned previously, the local recovery temperature for this configuration was calculated by assuming that the flow passed through a shock wave which was normal to the free-stream flow direction in contrast to the swept-shock method used for figure 10, and was then expanded to the modified Newtonian pressure. The differences between the swept-shock and normal-shock methods of calculating recovery temperature can be seen by comparing figures 11(a) with 12. The measured heat-transfer rates of these two figures are the same. However, the data of figure 12 were reduced by using a swept-shock recovery temperature and have higher values as well as more scatter. The temperature potential for these data $\left(T_r - T_w\right)$ varied from 150° to 250° F. The heat-transfer coefficients are, therefore, rather sensitive to errors in recovery temperature. It was thought that data reduced by using normal-shock entropy for the calculation of recovery temperature would be more accurate since this configuration had a blunt nose and was therefore bathed by a layer of air having the higher entropy. Note that both the data at a given station for different Reynolds numbers agree better and that the departure from theory is reduced when normal-shock entropy is used (fig. 11(a)). At higher angles of attack this layer of high-entropy air would become thinner over the leading edge and the advantage of using normal-shock recovery temperatures would possibly be lessened. The errors introduced by using swept-shock entropy to calculate recovery temperature at an angle of attack of 0° are shown by figure 12 to be as large as 20 percent.

One other anomaly in the data should be pointed out. In fig-
ures 11(b), 11(c), and 11(d) the data for large negative values of s/r
were obtained by testing the model at negative angles of attack and these
data are denoted in the same manner as were the data of the sharp-nose
configuration. Note that leading-edge data obtained at negative angles
of attack have higher heating rates near the nose than the data at cor-
responding values of s/r obtained at the positive angles of attack.
This is believed to be a result of the construction of the model. The
blunt-nose configuration was obtained by attaching a blunt-nose wing
section to the instrumented section of the sharp-nose configuration.
(See fig. 3.) The juncture of the cylindrical leading edge and the
spherical nose were faired together smoothly on the principal instru-
mented side of the leading edge and slab (windward side at positive angle
of attack). However, the opposite side of the nose and leading-edge junc-
ture were not faired as smoothly. Consequently, at negative angles of
attack the flow over the wing leading edge passed over this poor fairing
and was affected particularly near the nose. The data taken near the
nose at positive angles of attack are believed to be more valid than the
data of the same location taken at negative angles of attack.

The most important difference between these data and the data of
the sharp-nose model was that these data did show a trend in the varia-
tion of heat transfer with distance from the nose. In general, on the
windward portion of the leading edge, the heat-transfer rate was higher
for those stations nearer the nose. In addition, the low Reynolds num-
ber data had higher heat-transfer-coefficient ratios than the high Reynolds
number data. The variation with Reynolds number was also larger for those
stations nearer the nose.

Another difference indicated by these data was that the spherical-
nose model had laminar flow over a larger portion of the wing than did
the sharp-nose model.

SUMMARY OF RESULTS

Heat-transfer distributions have been measured for two cylindrical-
leading-edge, 70° swept slab wings, one having a sharp nose and the other
having a spherical nose. Tests were conducted at a Mach number of 6 and
Reynolds numbers of 3×10^4, 6×10^4, and 23×10^4, based on leading-edge
diameter. Angles of attack varied from -15° to 30° for the sharp-nose
configuration and from -15° to 20° for the spherical-nose configuration.

Results of these tests indicate the following:

1. Within the range of 3 to 6 leading-edge diameters from the nose,
the pressures and heating of the leading edge of the sharp-nose wing

appeared to be like that of an infinitely long swept cylinder up to an angle of attack of 20°. Within this range the heat-transfer coefficient can be predicted by an easily applied theory with reasonable accuracy. At angles of attack of 25° and 30°, the high Reynolds number data of the windward side of the leading edge are either transitional or turbulent and the measured heat-transfer rates are therefore much higher than the theoretical values.

2. On the flat portion of the sharp-nose wing, the data indicated transitional flow at angles of attack from 0° to 30°.

3. The flow over the spherical-nose wing was laminar over a larger portion of the wing than for the sharp-nose wing.

4. The heat-transfer rate to the leading edge of the spherical-nose wing varied with distance from the nose. Within a range of 2 to 5 leading-edge diameters from the nose, the heat-transfer rates were higher for locations nearer the nose. In addition, the lower Reynolds number data had higher heat-transfer-coefficient ratios than the high Reynolds number data. This variation with Reynolds number was also larger for locations nearer the nose.

5. The pressure distribution around the cylindrical leading edge was predicted with reasonable accuracy by modified Newtonian theory for both wings.

Langley Research Center,
     National Aeronautics and Space Administration,
          Langley Air Force Base, Va., February 19, 1962.

REFERENCES

1. Lees, Lester: Laminar Heat Transfer Over Blunt-Nosed Bodies at Hypersonic Flight Speeds. Jet Propulsion, vol. 26, no. 4, April 1956, pp. 259-269, 274.

2. Beckwith, I. E., and Cohen, N. B.: Application of Similar Solutions to Calculations of Laminar Heat Transfer on Bodies With Yaw and Large Pressure Gradients in High-Speed Flow. NASA TN D-625, 1961.

3. Beckwith, Ivan E., and Gallagher, James J.: Local Heat Transfer and Recovery Temperatures on a Yawed Cylinder at a Mach Number of 4.15 and High Reynolds Numbers. NASA TR R-104, 1961. (Supersedes NASA MEMO 2-27-59L.)

4. Bertram, Mitchel H., Feller, William V., and Dunavant, James C.: Flow Fields, Pressure Distributions, and Heat Transfer for Delta Wings at Hypersonic Speeds. NASA TM X-316, 1960.

5. Jones, Robert A., and Gallagher, James J.: Heat-Transfer and Pressure Distributions of a 60° Swept Delta Wing With Dihedral at a Mach Number of 6 and Angles of Attack From 0° to 52°. NASA TM X-544, 1961.

6. Rhudy, J. P., Hiers, R. S., and Rippey, J. O.: Pressure Distribution and Heat Transfer Tests on Two Fin-Flat Plate Interference Models and Several Blunt Leading Edge Delta Wing Models. AEDC-TN-60-168(Contract No. AF 40(600)-800 S/A 11(60-110)), Arnold Eng. Dev. Center, Sept. 1960.

7. Hiers, R. S., and Hillsamer, M. E.: Heat Transfer and Pressure Distribution Tests on a Blunted Delta Wing and Several Body, Elevon, and Fin Attachments. AEDC-TN-60-238 (Contract No. AF 40(600-800 S/A 11(60-110)), Arnold Eng. Dev. Center, Jan. 1961.

8. Bertram, Mitchel H., and Henderson, Arthur, Jr.: Recent Hypersonic Studies of Wings and Bodies. ARS Jour., vol. 31, no. 8., Aug. 1961, pp. 1129-1139.

9. Beckwith, Ivan E.: Similar Solutions for the Compressible Boundary Layer on a Yawed Cylinder With Transpiration Cooling. NACA TR R-42, 1959. (Supersedes NACA TN 4345.)

14

L-1452

Station A

Station B

Station C

Station D

Station E

1-1/2 R

20°

2-7/8

Note: 49 thermocouples located in five rows
(A, B, C, D, and E) at $\theta = -15^{\circ}$, 0°, 15°,
30°, 45°, 60°, 75°, and 90°, and at
$y = 0.2$ in., 0.6 in., 1.0 in., and 1.5 in.
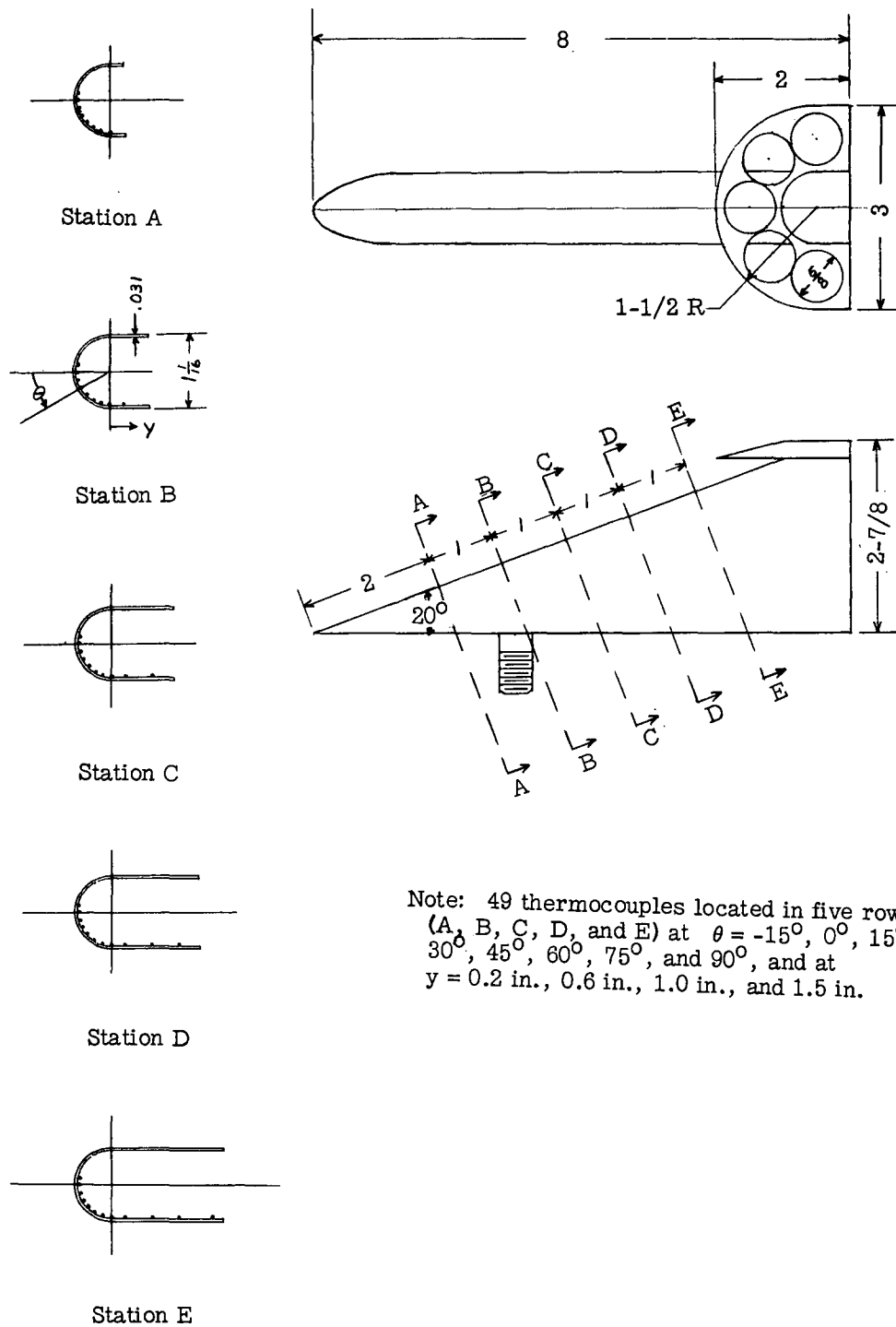
Figure 1.- Sketch of semispan model showing thermocouple locations for
both models. (All dimensions are in inches.)
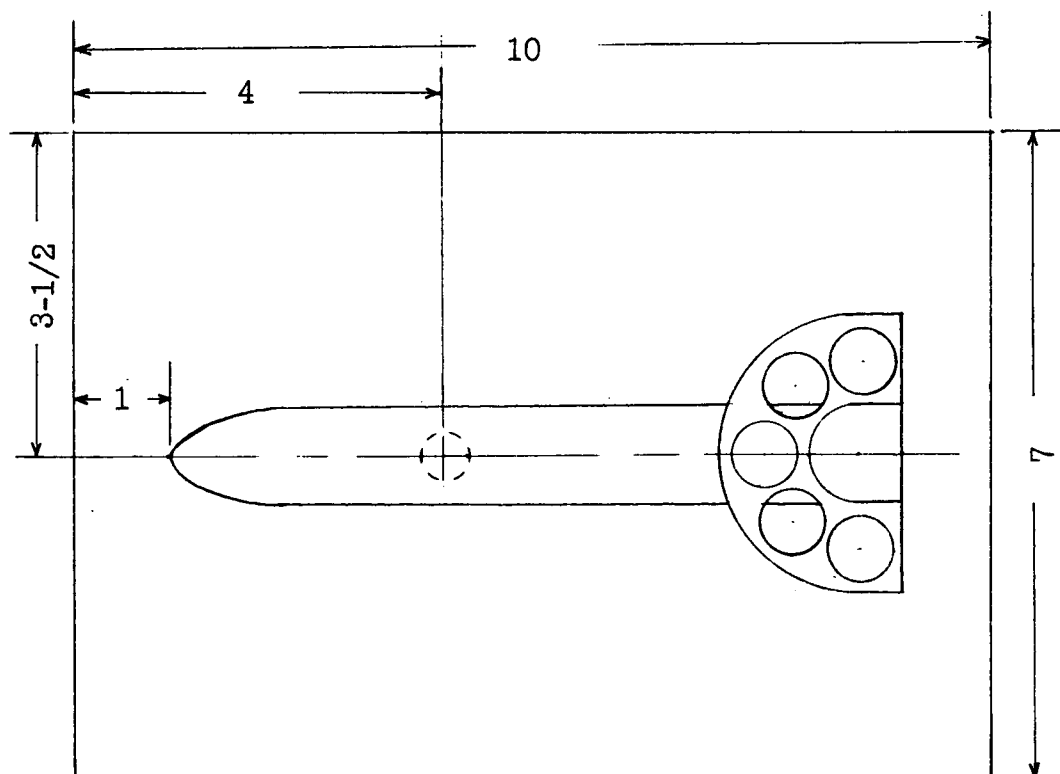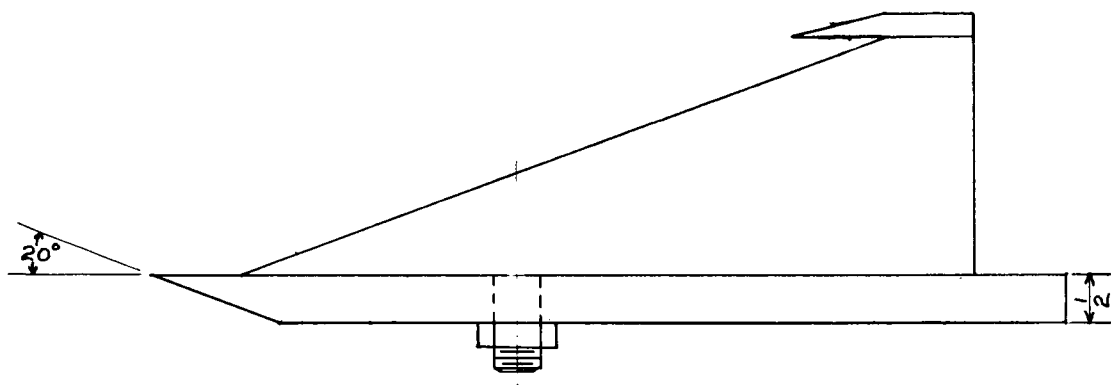
Figure 2.- Sketch of semispan model showing location on plate.
(All dimensions are in inches.)

Station B

Station C

Station D

Station E

17/32 R

1-1/16

1/8

θ

y

8-17/32

2

3

17/32 R

1-1/2 R

3

20°

20°

1-17/32

1

1

1

1

1

1

1

1

1

2-7/8

2-1/2

B

C

D

E

x

Note: 28 pressure orifices located in four rows
(B, C, D, and E) at θ = -15°, 0°, 15°, 30°,
45°, and 90°, and at y = 0.5 in. Six pressure
orifices located on center line.
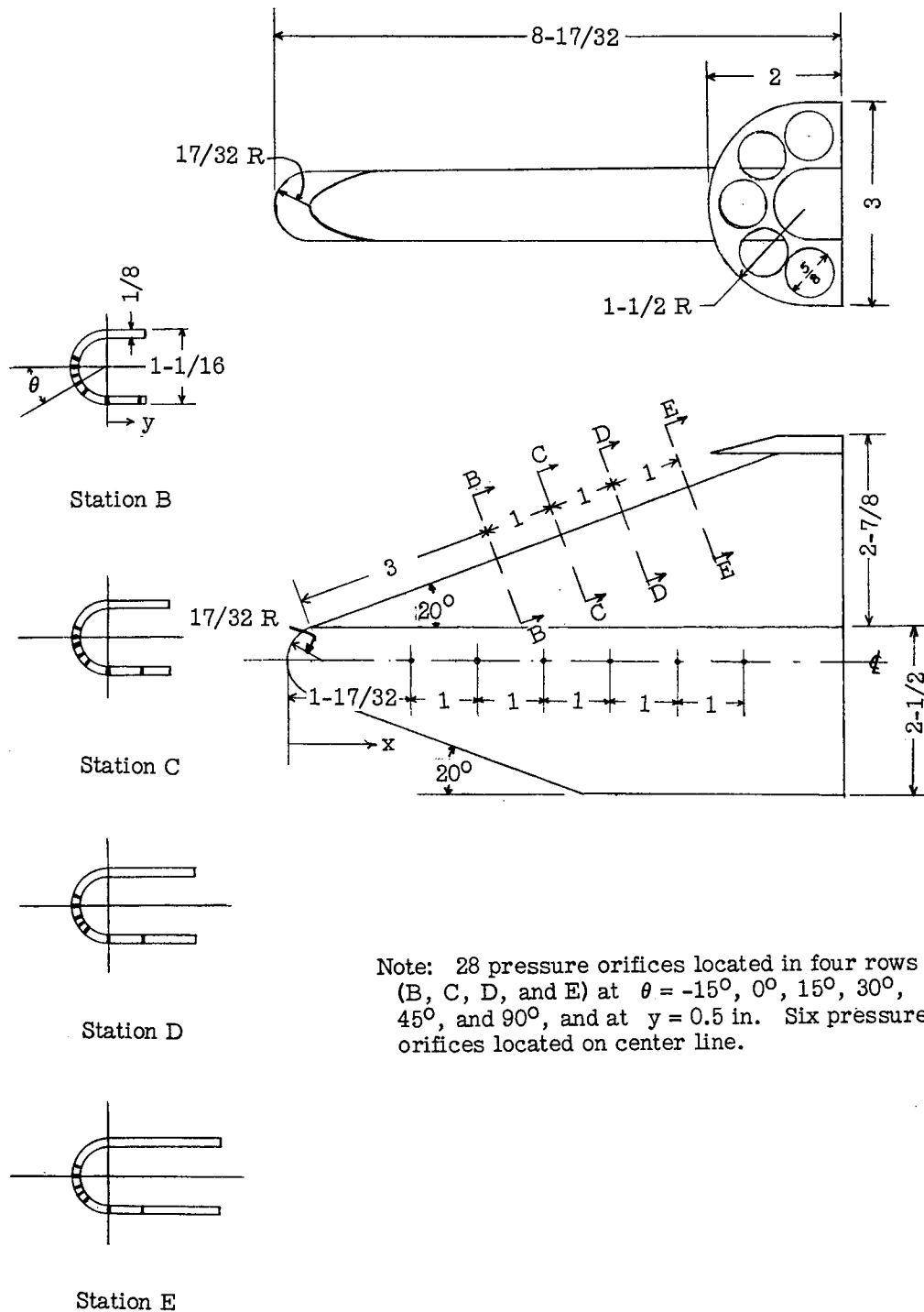
Figure 3.- Sketch of 3/4-span model showing pressure orifice locations.
(All dimensions are in inches.)
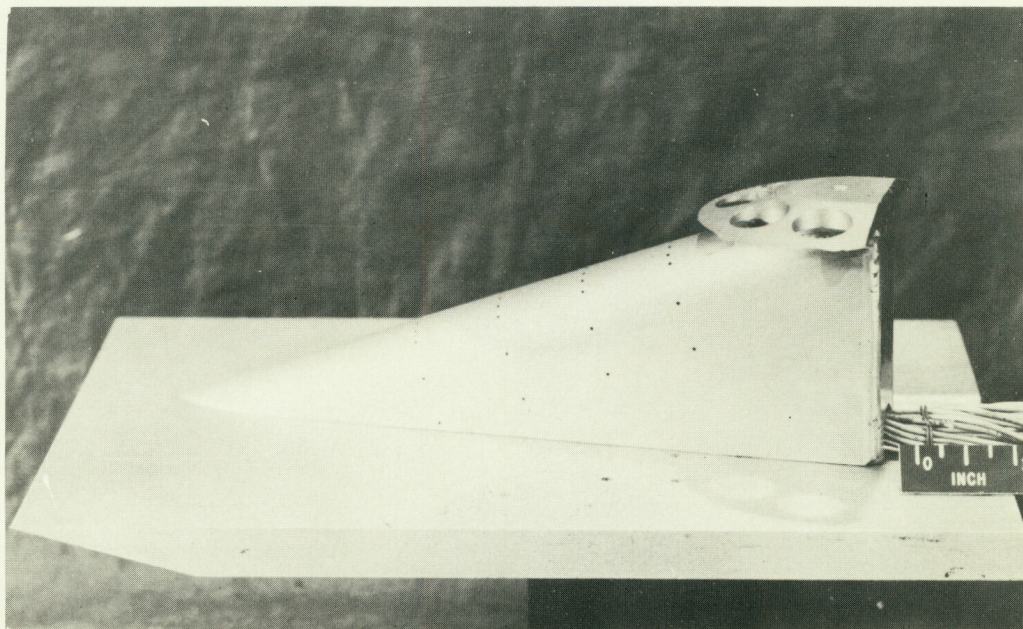
L-1452

(a) Sharp-nose configuration.
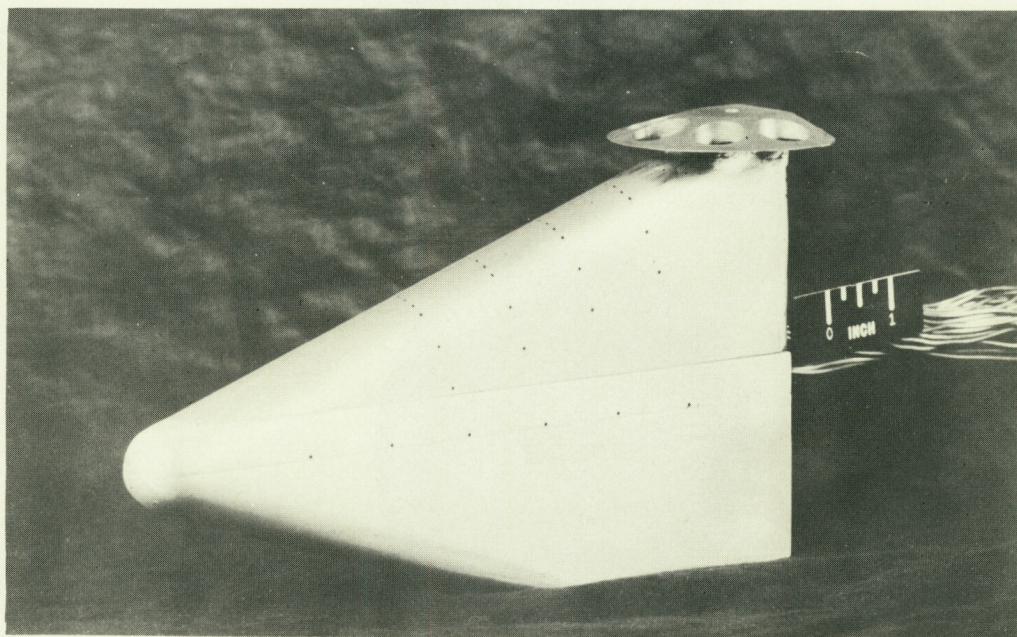
(b) Spherical-nose configuration.

L-62-44

Figure 4.- Photographs of models.
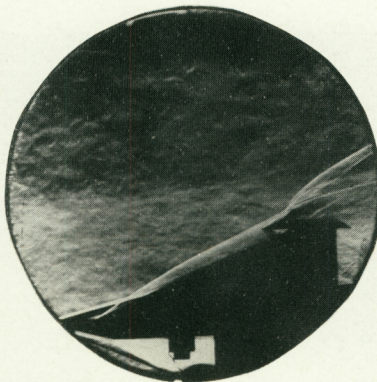
L-1452

$\alpha = 30°$
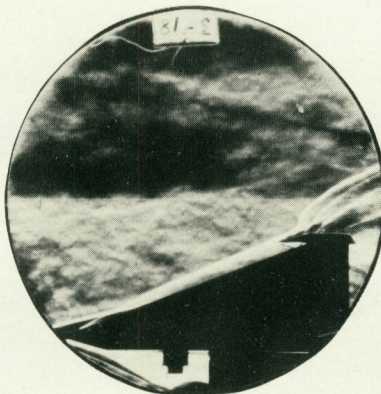
$\alpha = 15°$
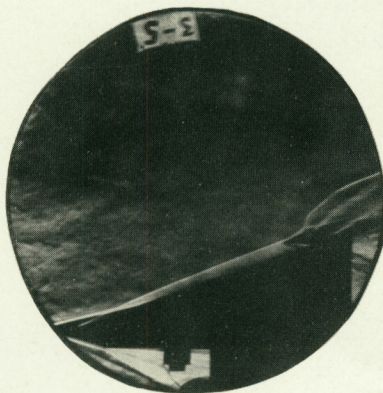
$\alpha = 0°$ L-62-46

Figure 5.- Schlieren photographs of sharp-nose configuration.
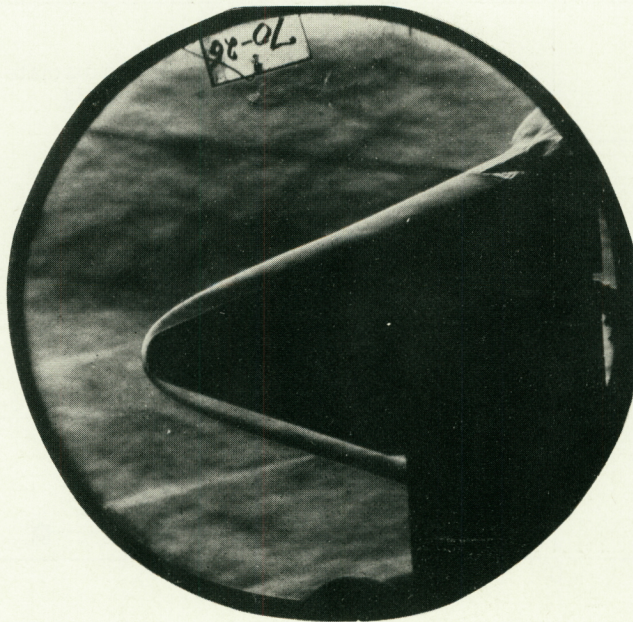
$\alpha = 15^{\circ}$
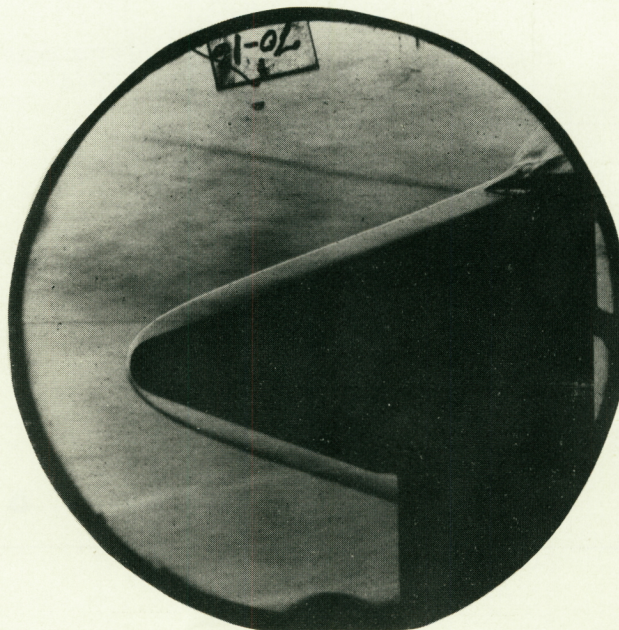
$\alpha = 0^{\circ}$ L-62-45

Figure 6.- Schlieren photographs of spherical-nose configuration.
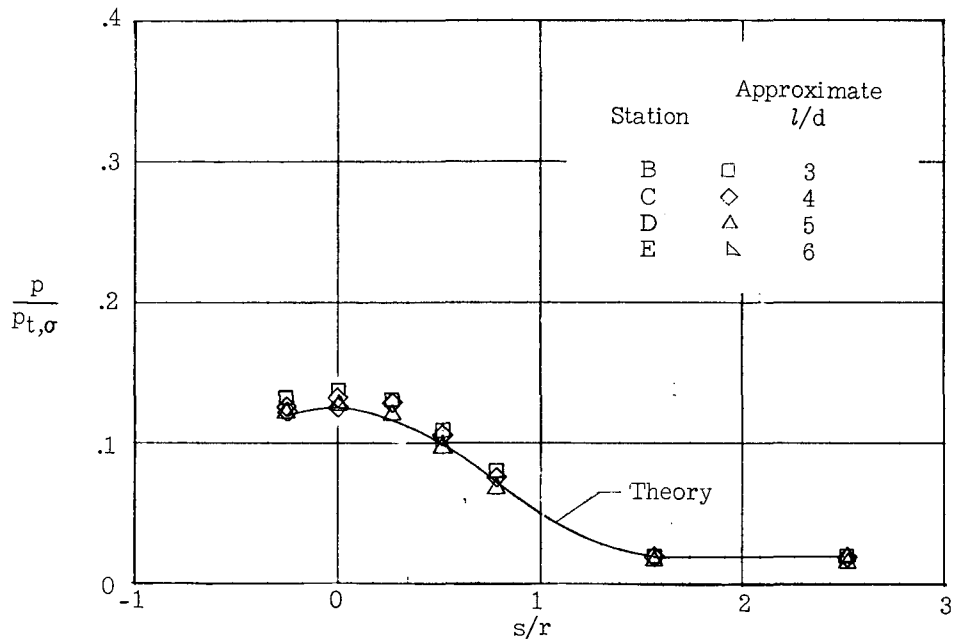
(a) $\alpha = 0^{\circ}$.
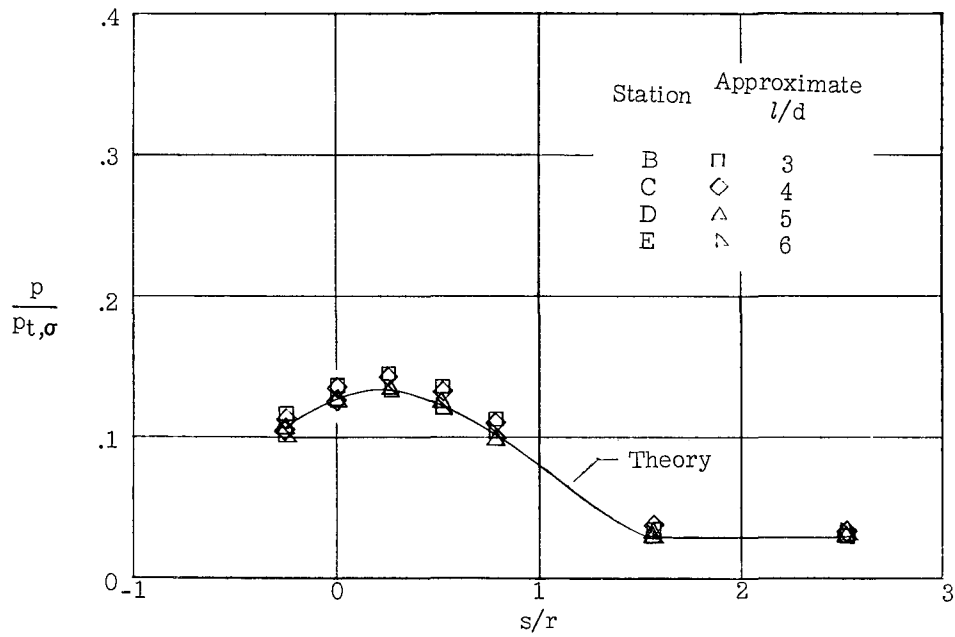
(b) $\alpha = 5^{\circ}$.

Figure 7.- Pressure distributions of sharp-nose configuration $\left(R_d = 75 \times 10^4 \right)$.

L-1452
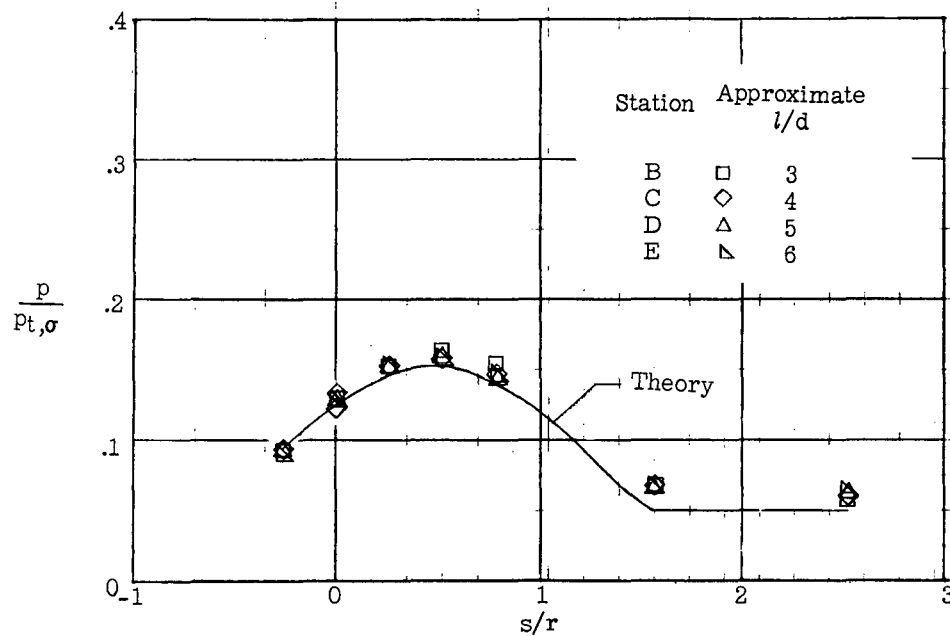
(c) $\alpha = 10^{\circ}$.
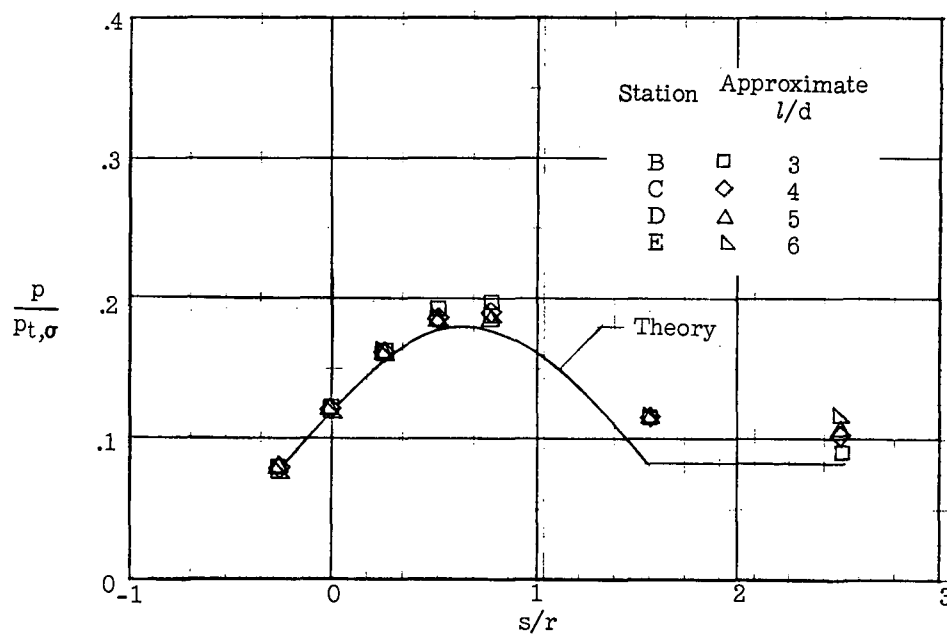
(d) $\alpha = 15^{\circ}$.

Figure 7.- Continued.
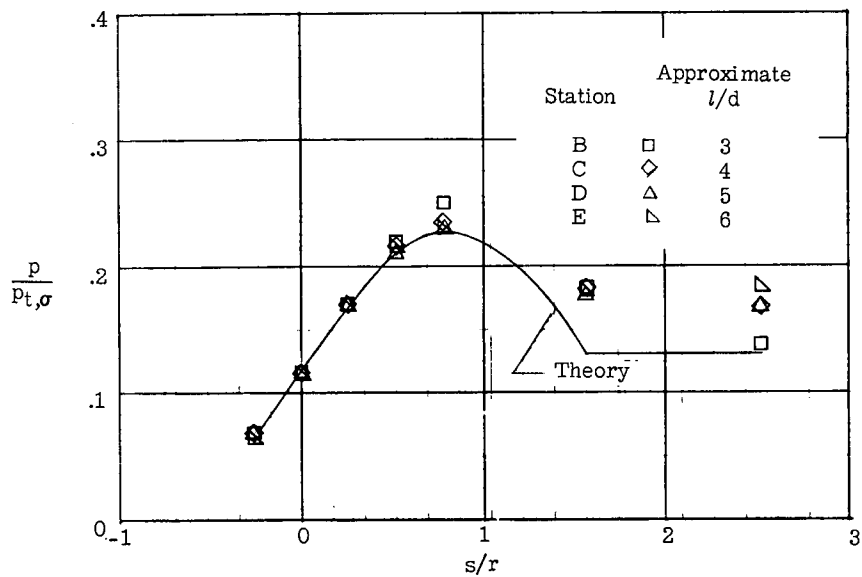
(e) $\alpha = 20^{\circ}$.
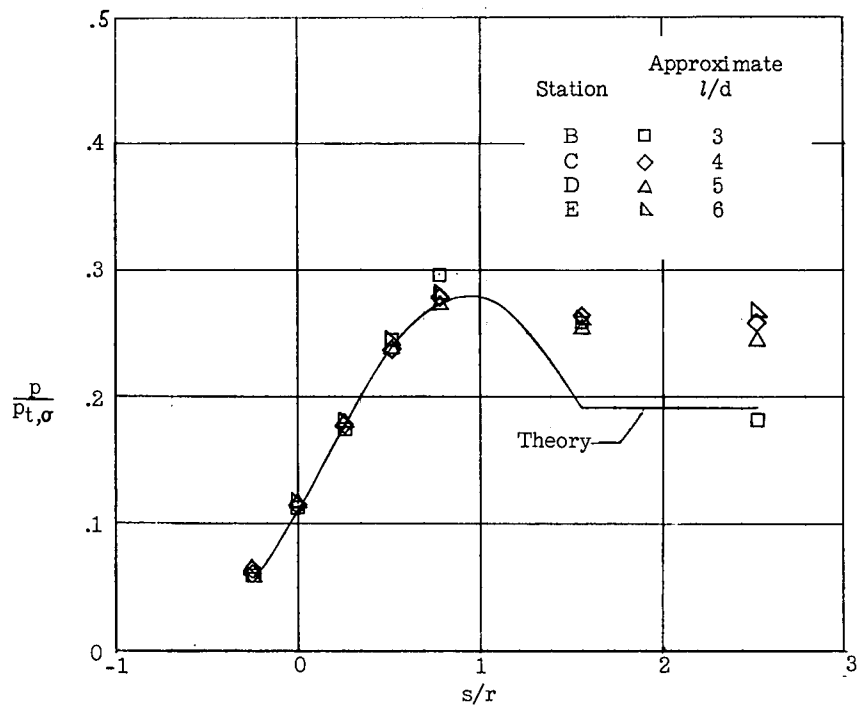
(f) $\alpha = 25^{\circ}$.

Figure 7.- Continued.
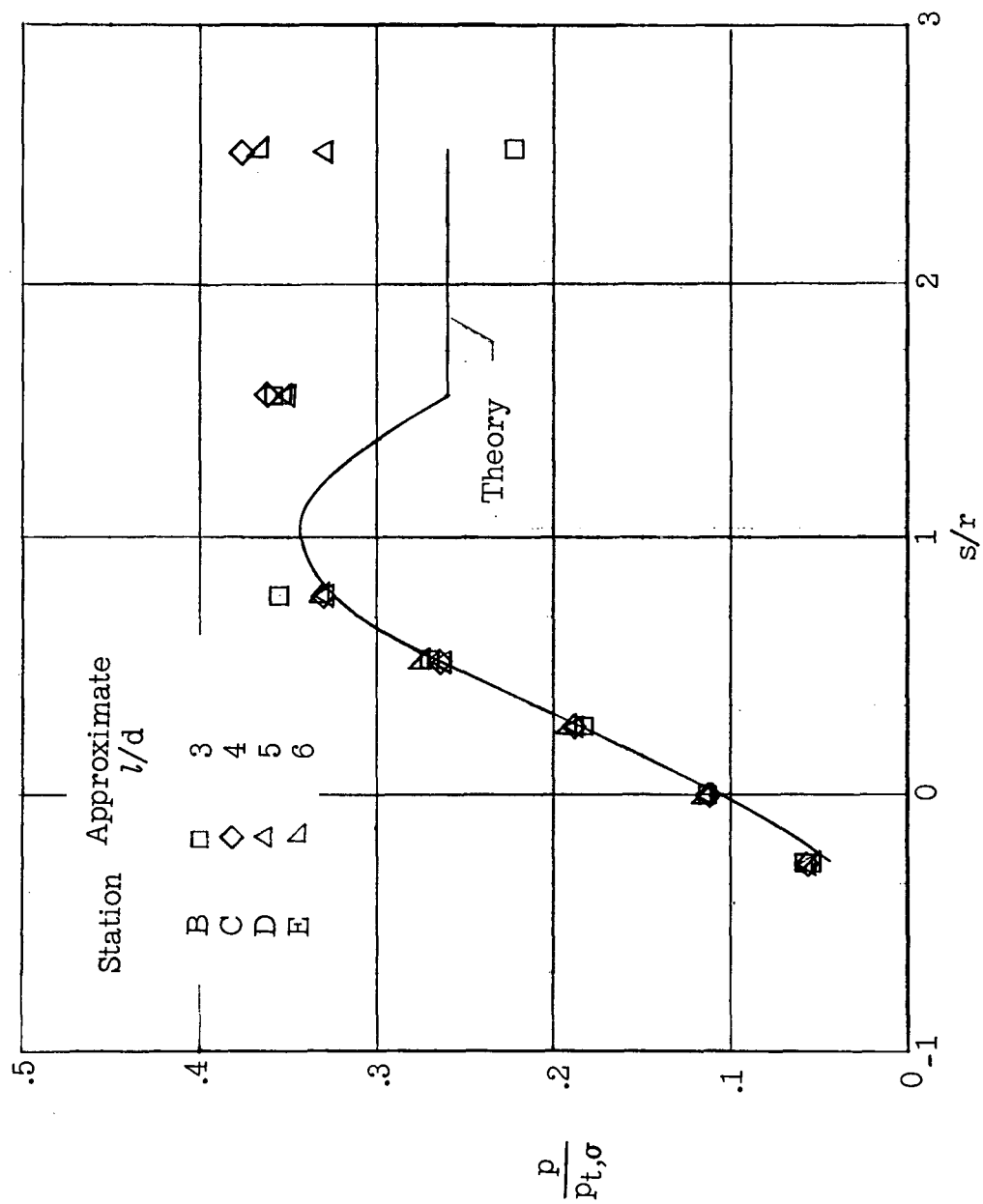
(g) α = 30°.

Figure 7.- Concluded.
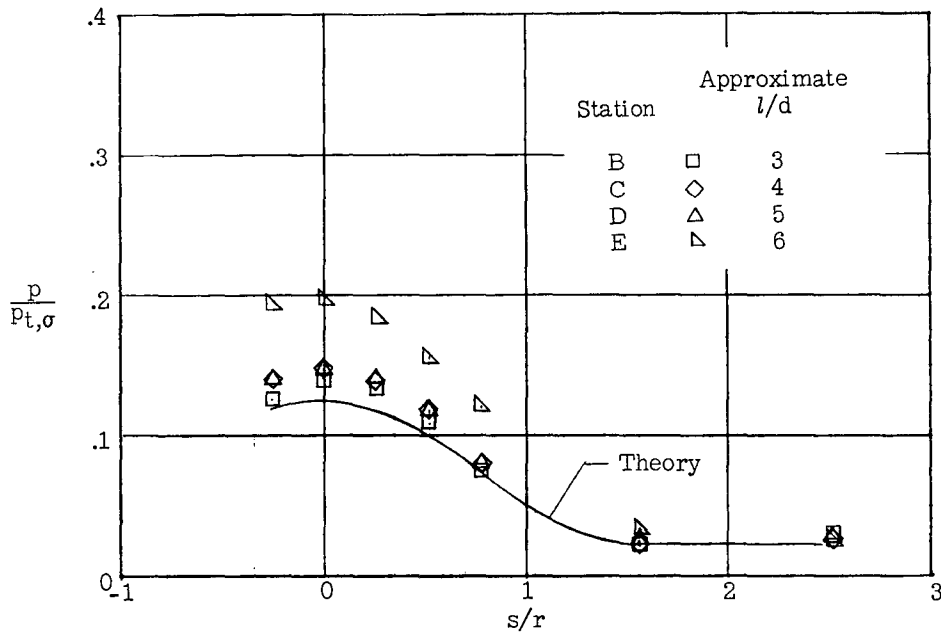
(a) $\alpha = 0^\circ$.
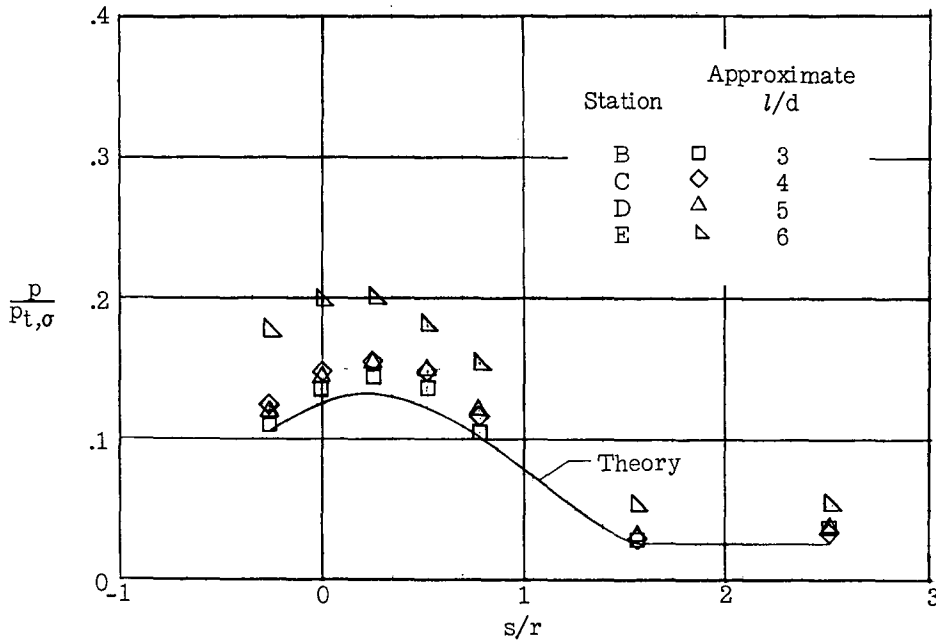
(b) $\alpha = 5^\circ$.

Figure 8.- Pressure distributions of spherical-nose configuration $\left(R_d = 75 \times 10^4 \right)$.

L-1452

L-1452
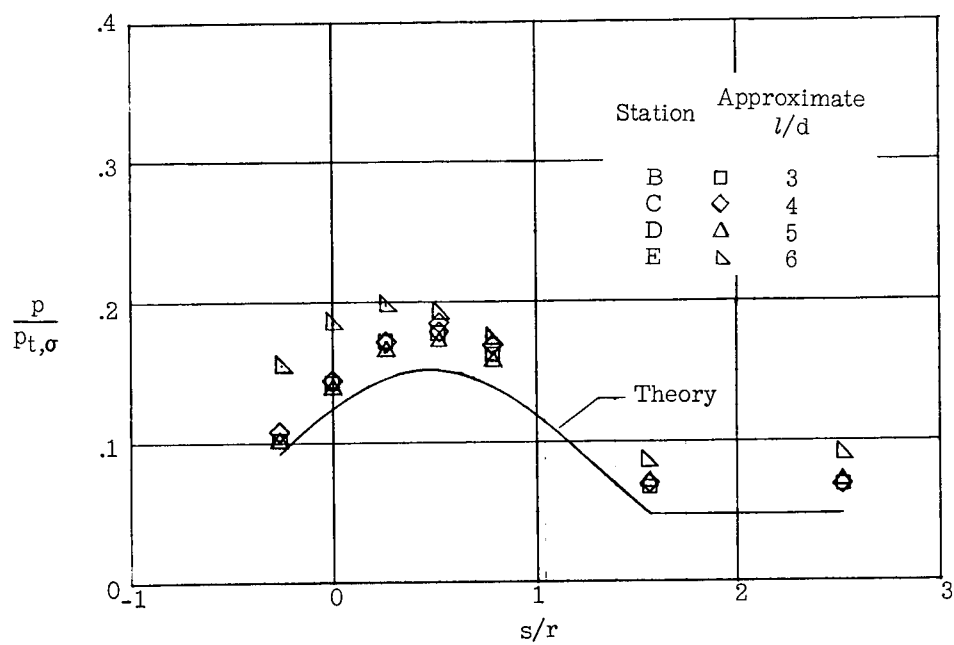
(c) $\alpha = 10^{\circ}$.
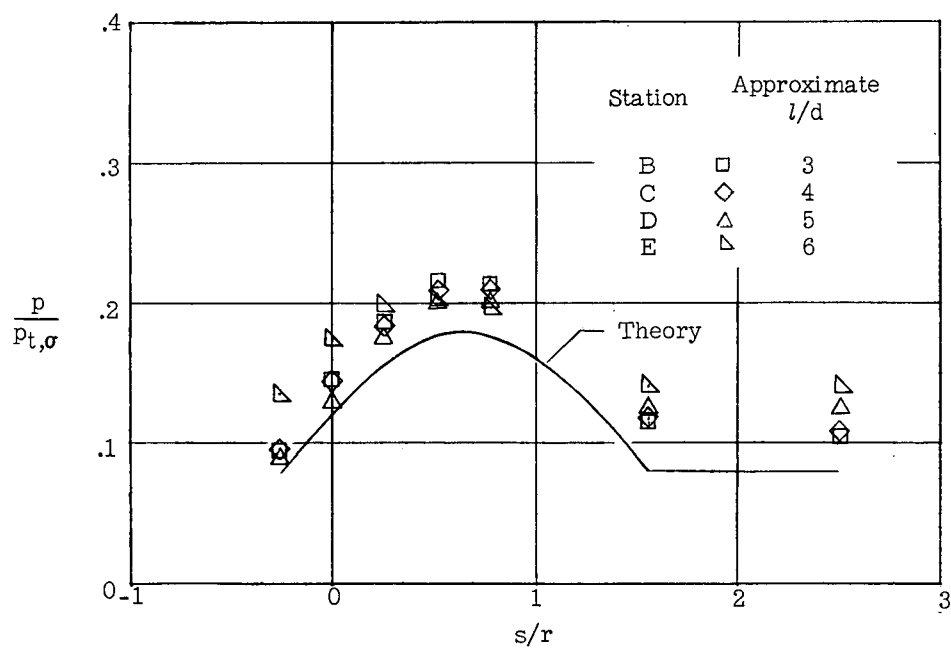
(d) $\alpha = 15^{\circ}$.

Figure 8.- Continued.
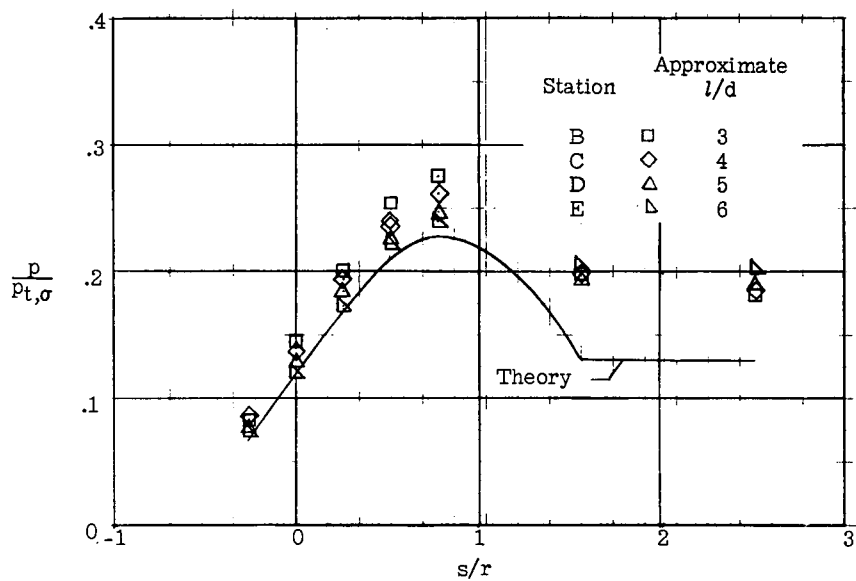
(e) $\alpha = 20°$.

(f) $\alpha = 25°$.

Figure 8.- Concluded.

27

L-1452

α , deg

25

20

15

10

5

0

.4

.3

.2

.1

0

0   1   2   3   4   5   6   7

$\dfrac{p}{p_{t,\sigma}}$

x, in.
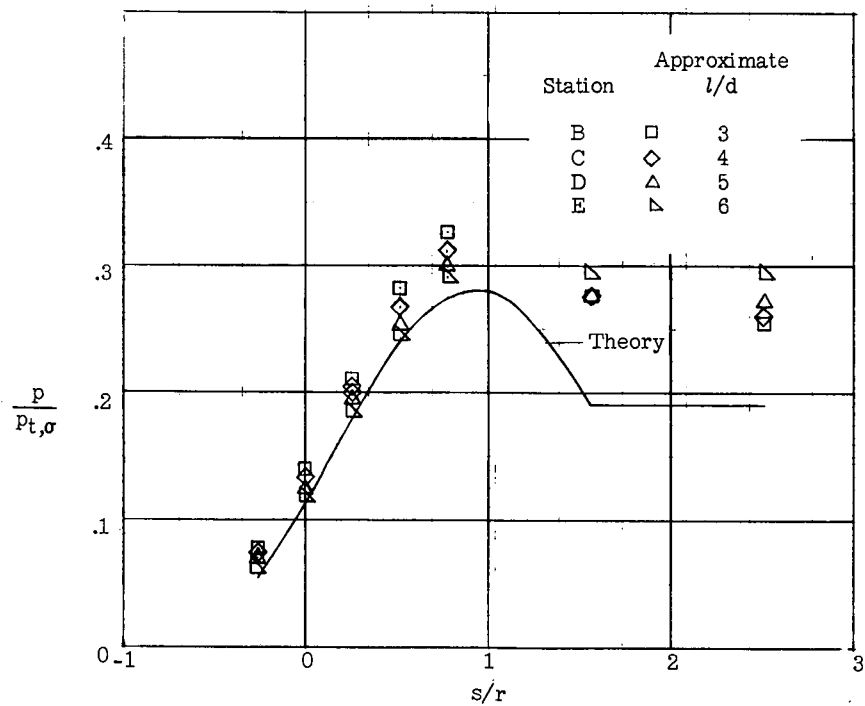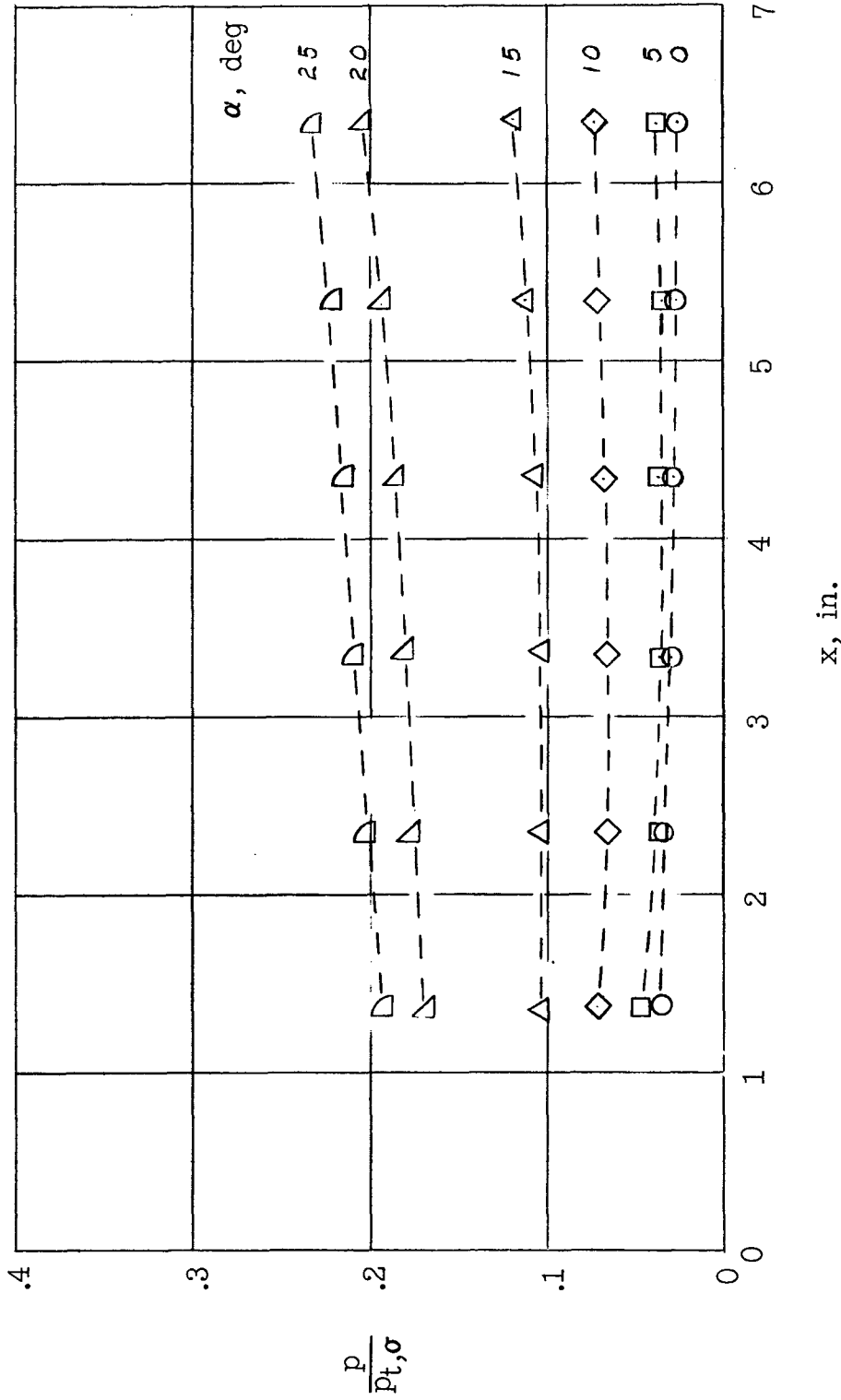
Figure 9.- Center-line pressure distribution.
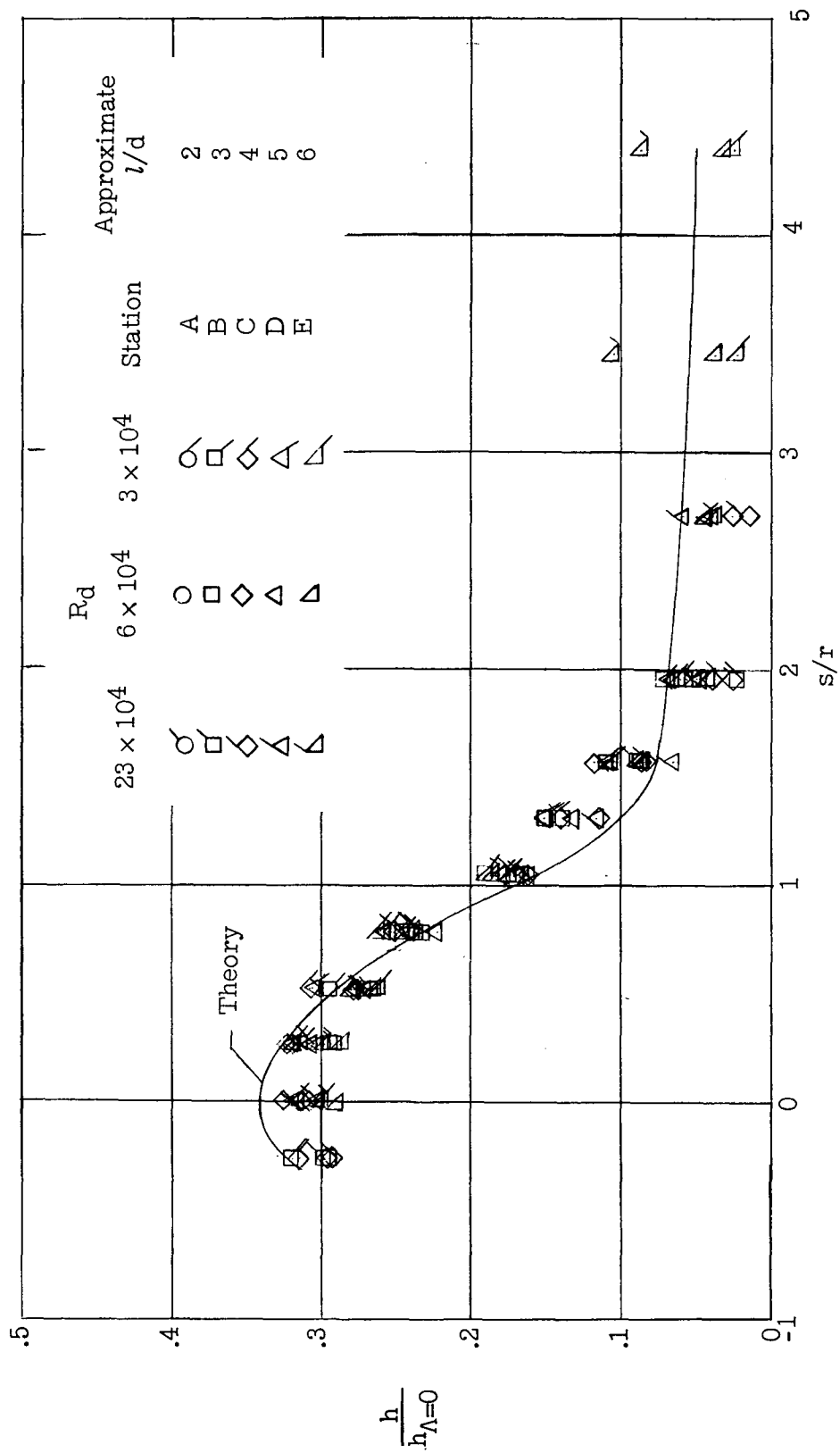
(a) $\alpha = 0°$.

Figure 10.- Heat-transfer distributions of sharp-nose configuration.

L-1452

(b) α = 5°.

Figure 10.- Continued.

L-1452
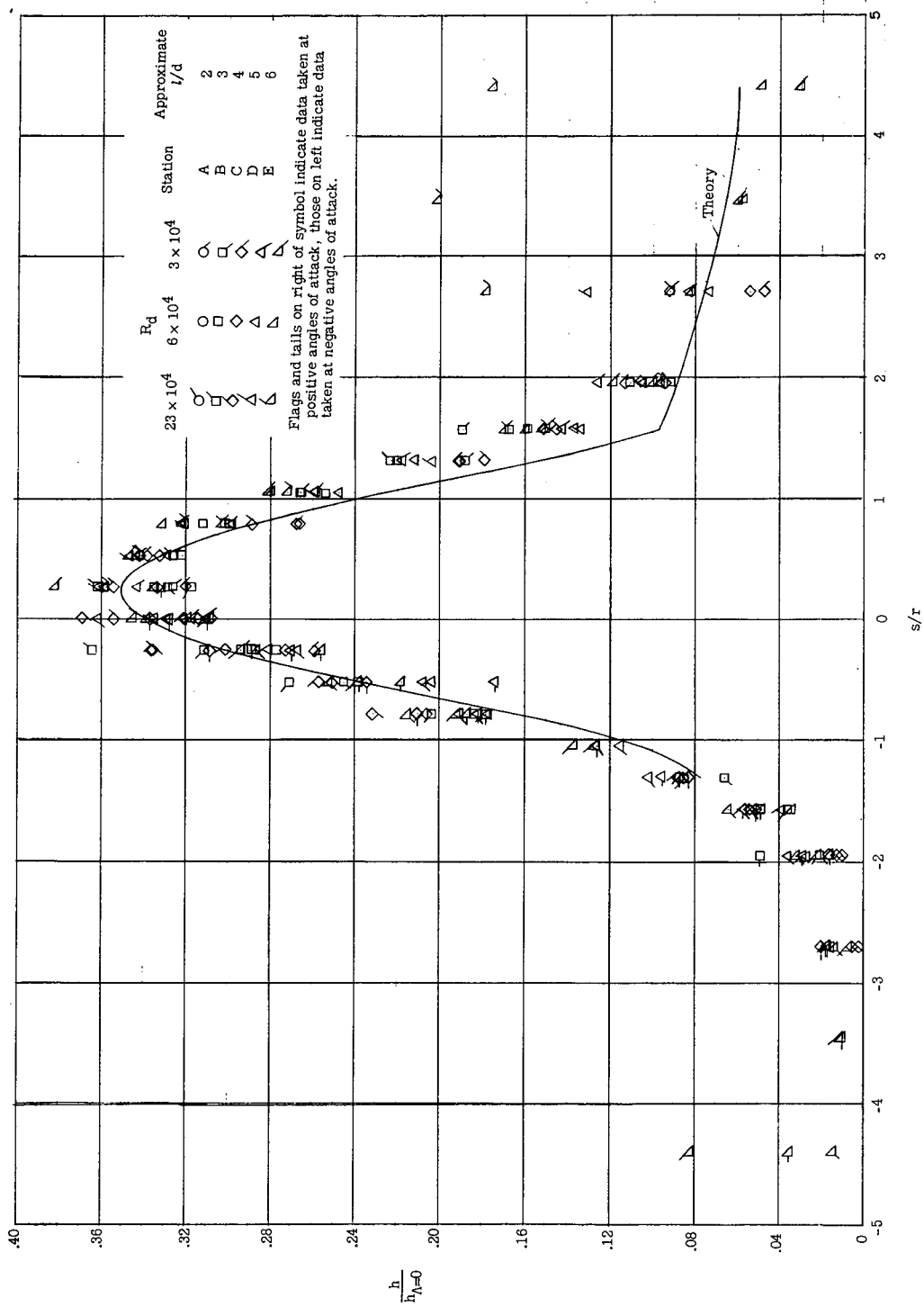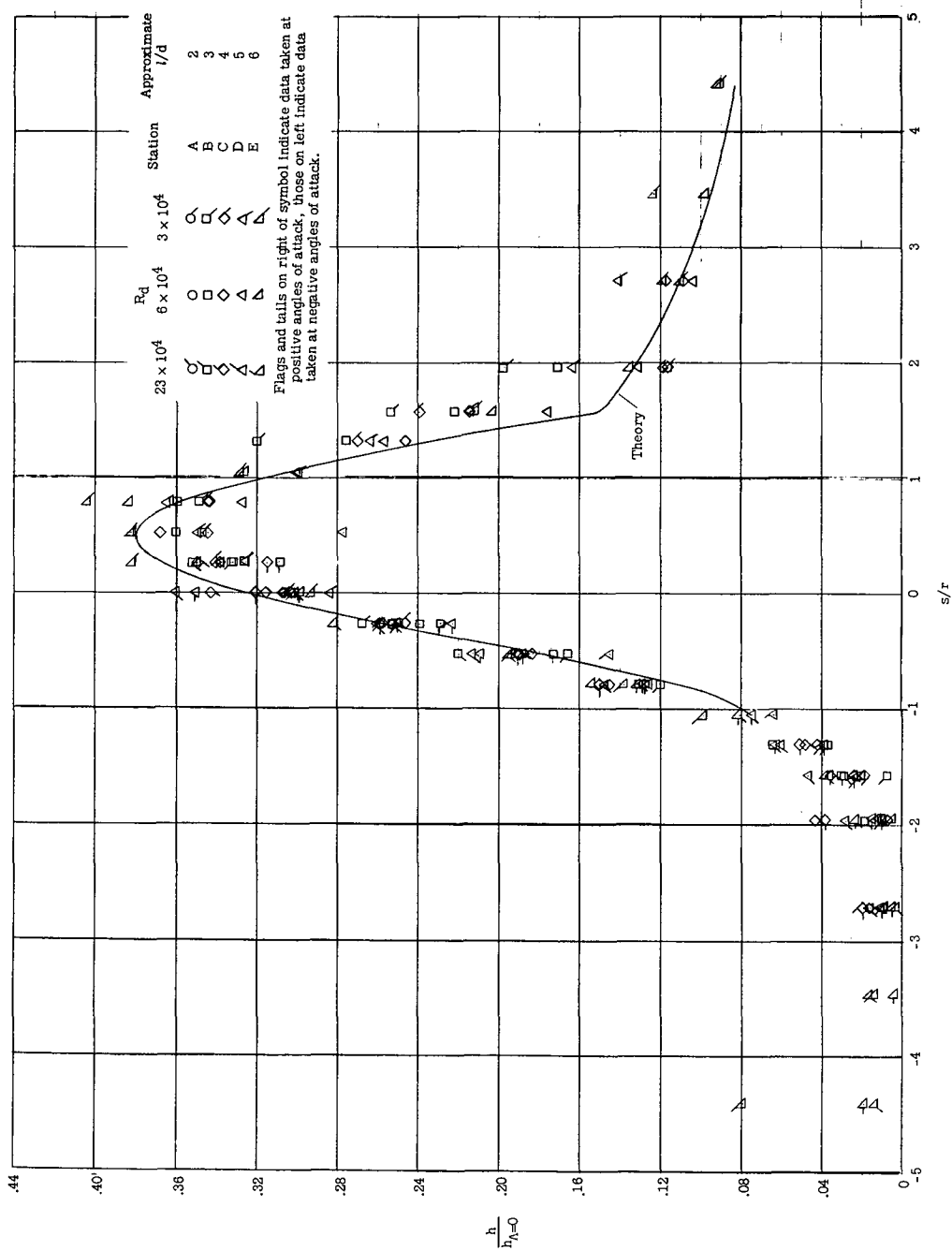
(c) α = 10°.

Figure 10.- Continued.

L-1452
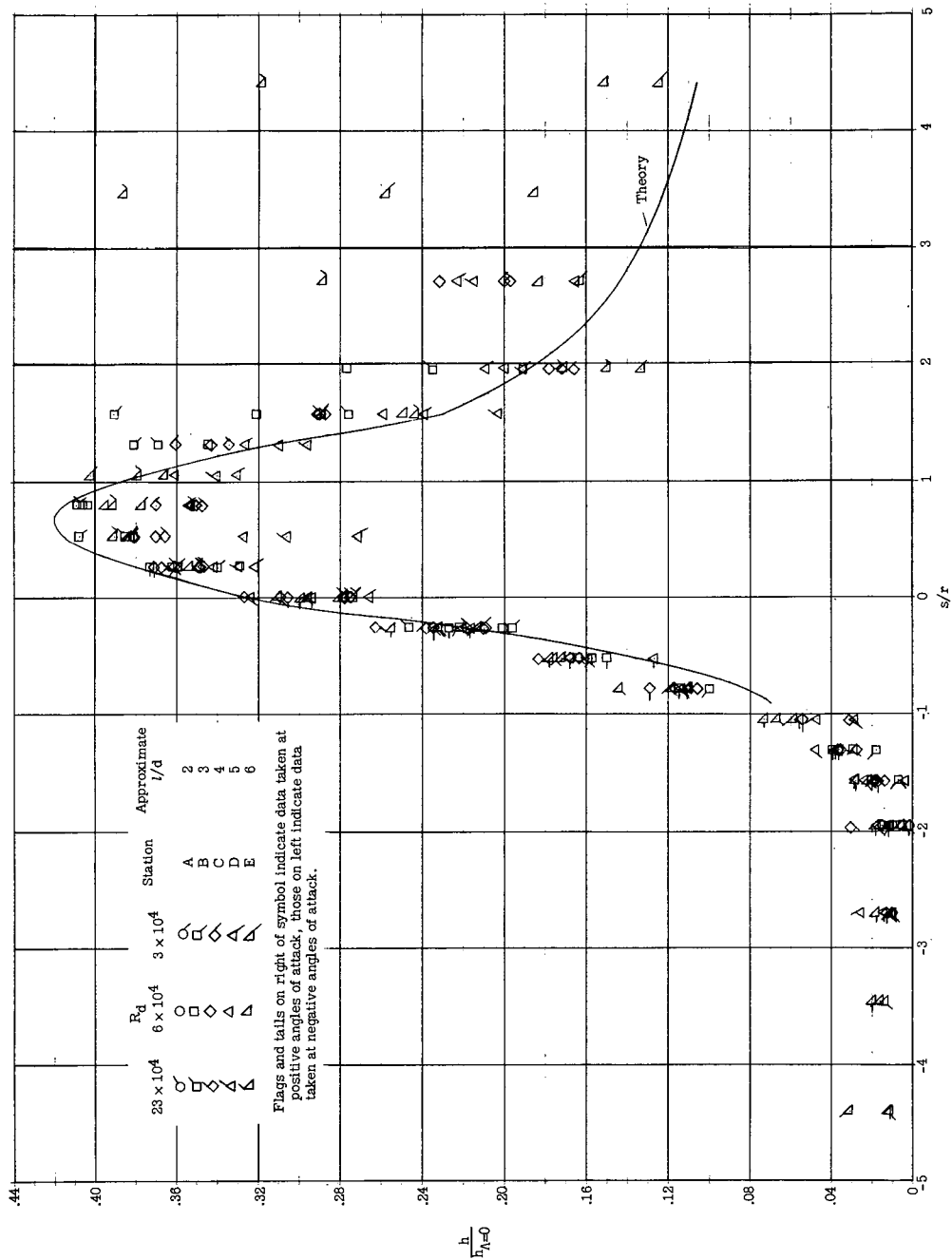
(d) α = 15°.

Figure 10.- Continued.
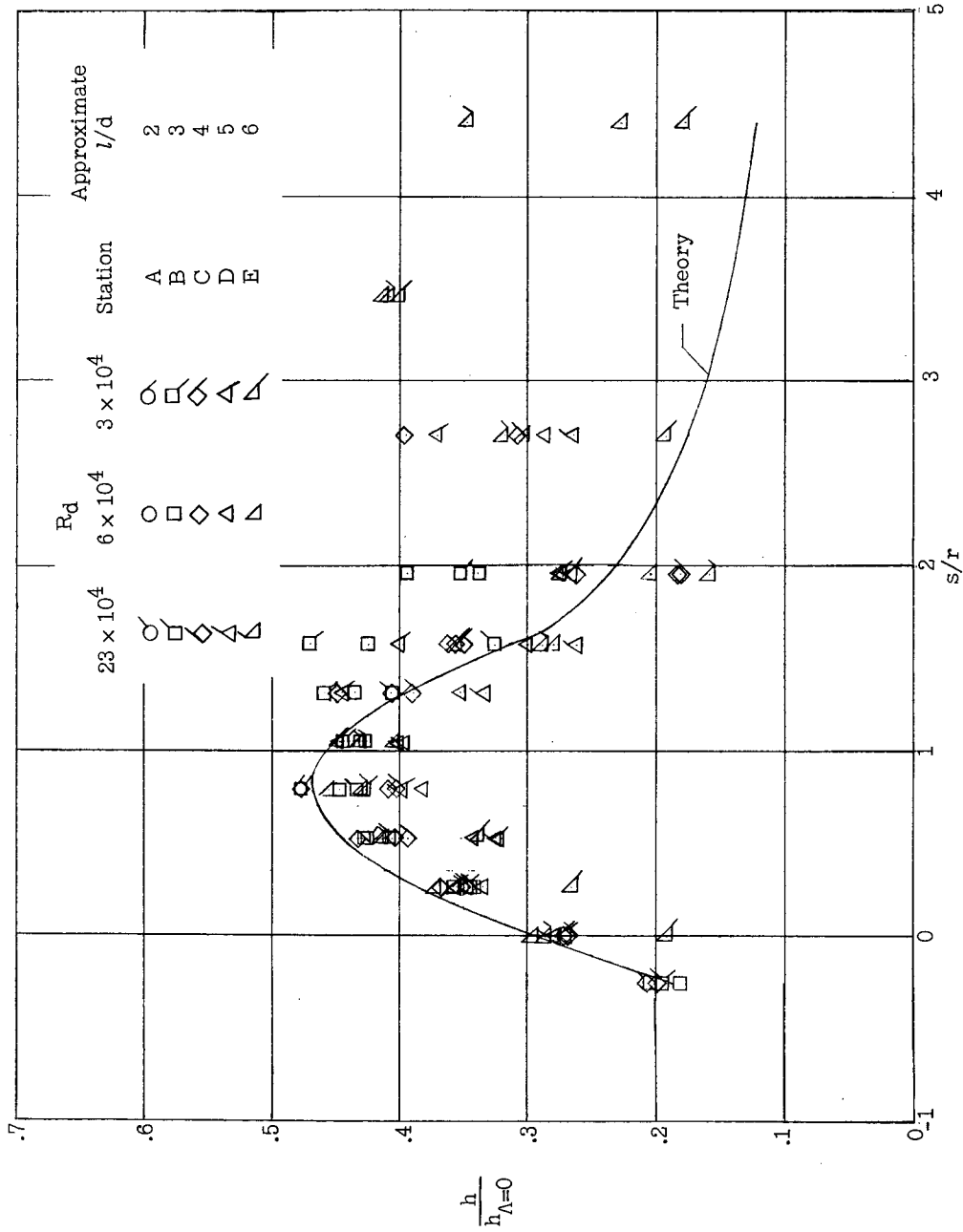
(e) α = 20°.

Figure 10.- Continued.

L-1452
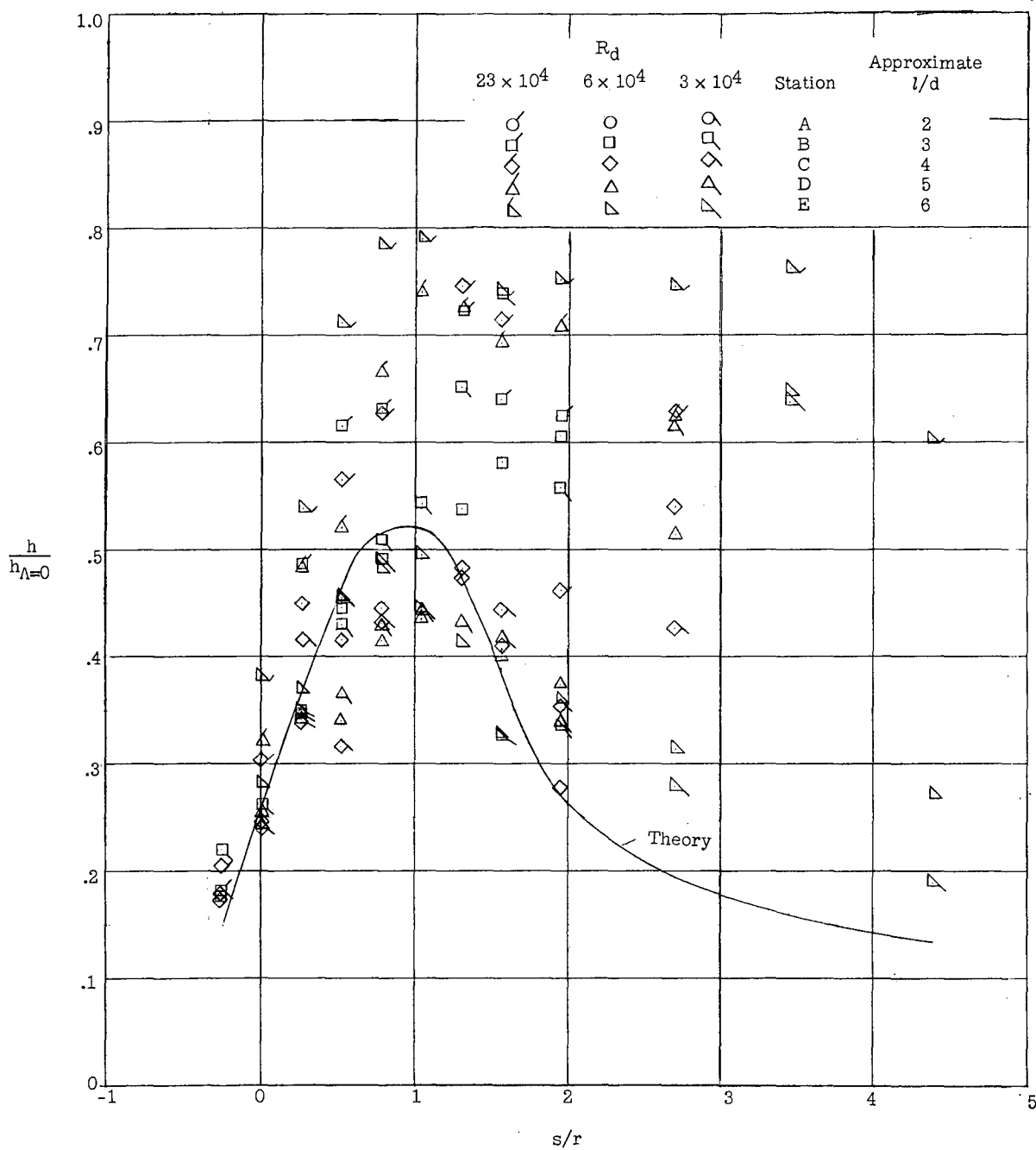
(f) $\alpha = 25°$.

Figure 10.- Continued.
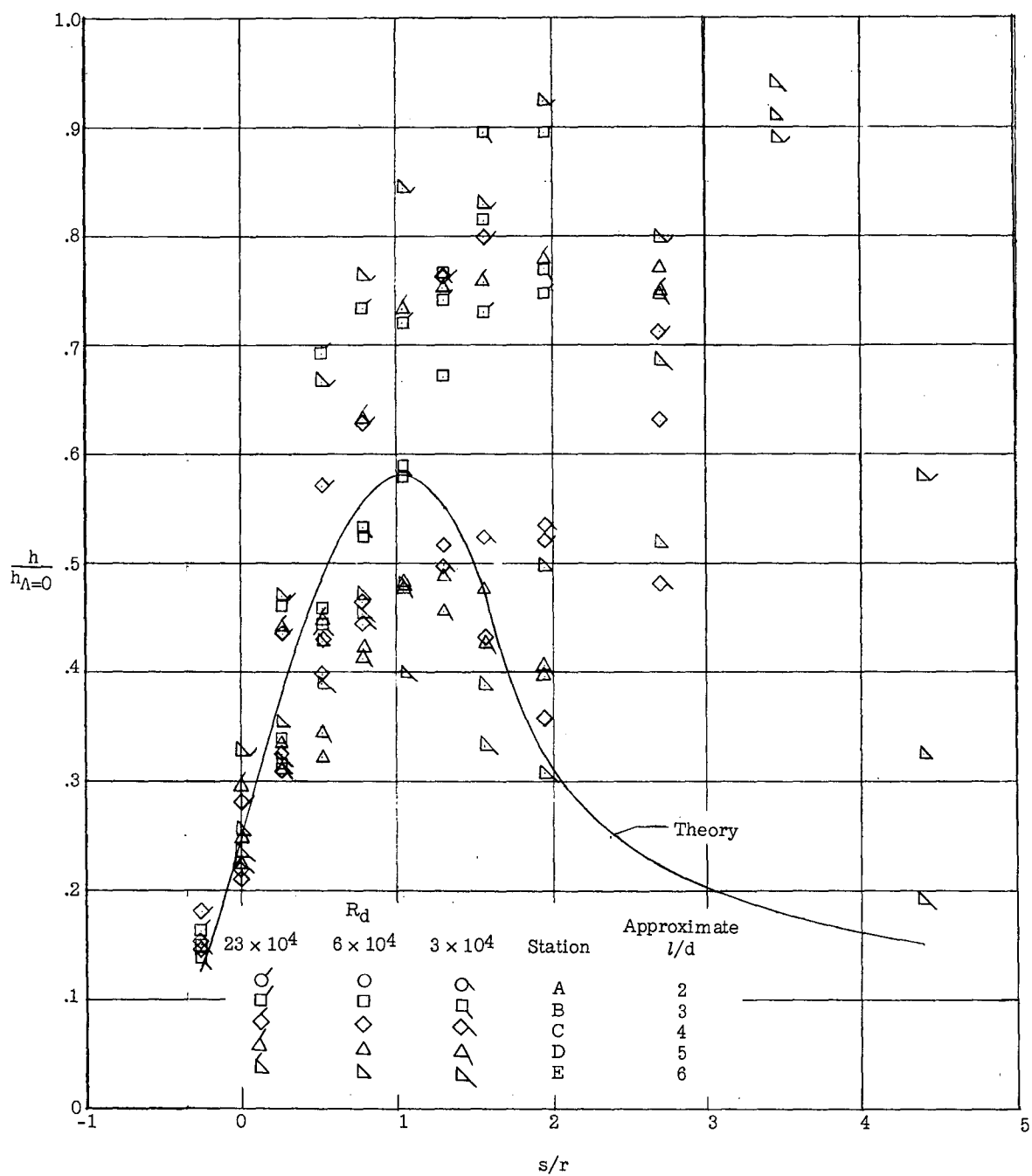
(g) α = 30°.

Figure 10.- Concluded.
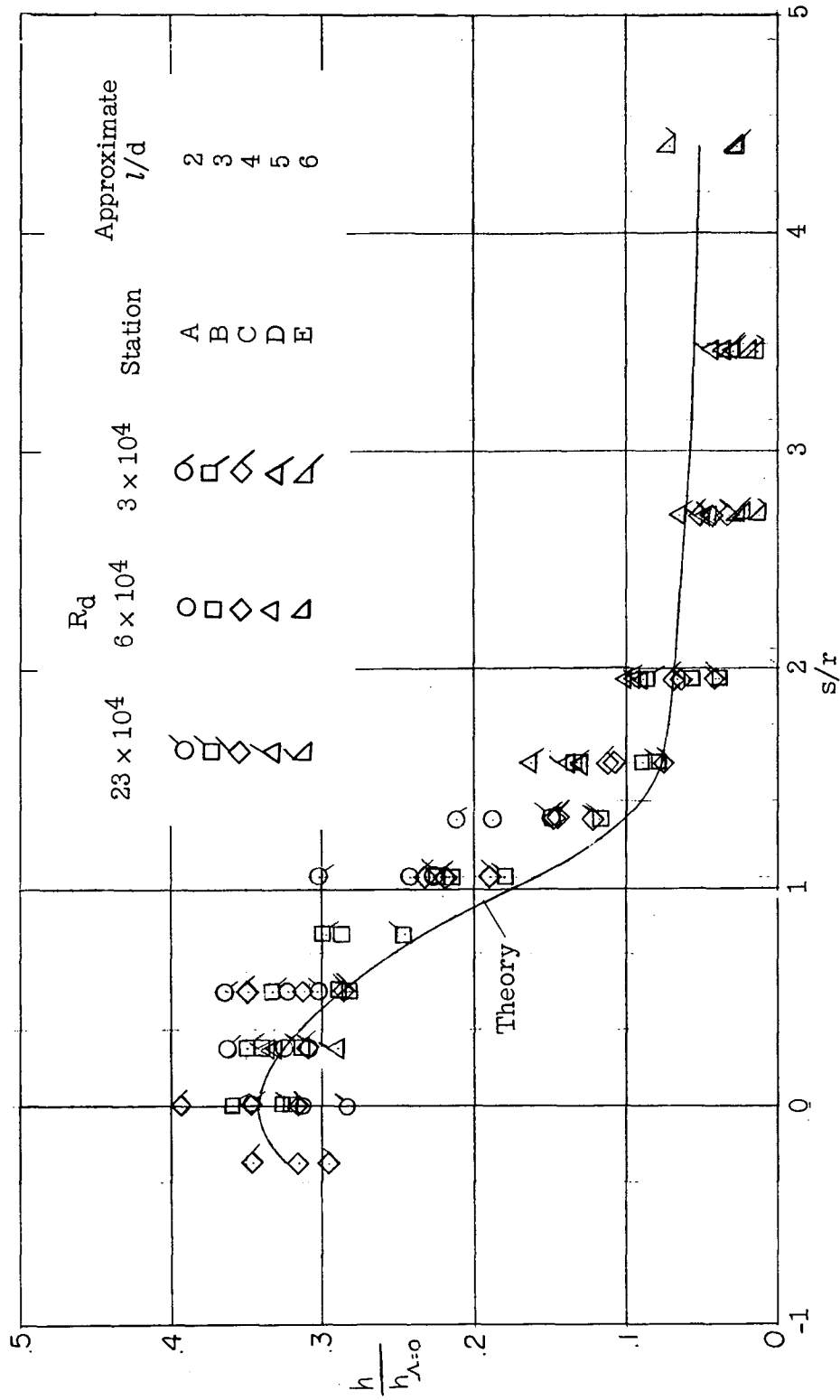
Figure 11.- Heat-transfer distributions of spherical-nose configuration.

(a) $\alpha = 0°$.

35

(b) α = 5°.

Figure 11.- Continued.

L-1452

L-1452

(c) $\alpha = 10^{\circ}$.

Figure 11.- Continued.

(d) α = 15°.

Figure 11.- Continued.

L-1452

L-1452

Approximate
l/d

Station   2
A   3
B   4
C   5
D   6
E

R.

3 × 10⁴

6 × 10⁴

23 × 10⁴

Theory

$\dfrac{h}{h_{\Lambda=0}}$

.6

.5

.4

.3

.2

.1

0.

-1   0   1   2   3   4   5

s/r
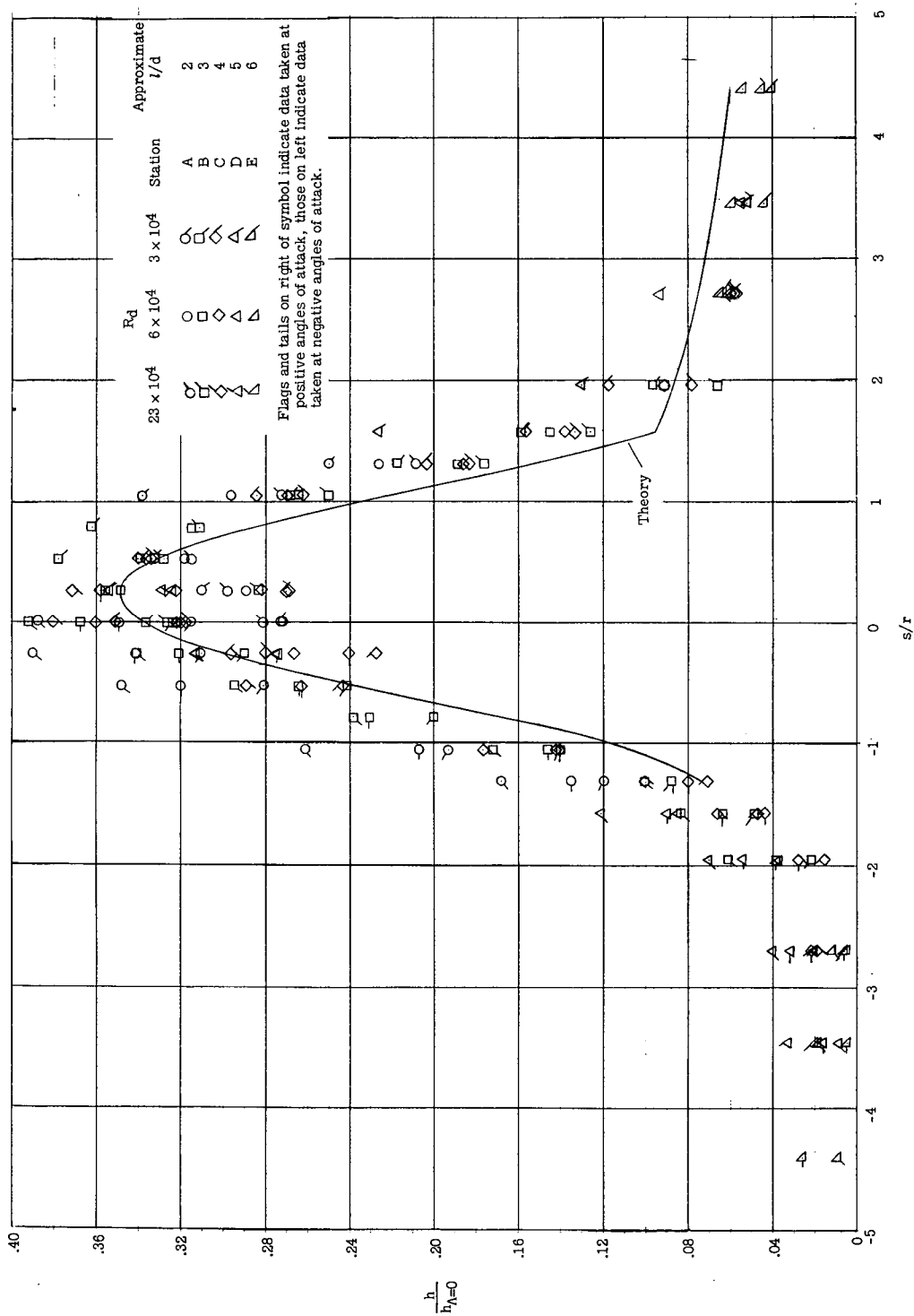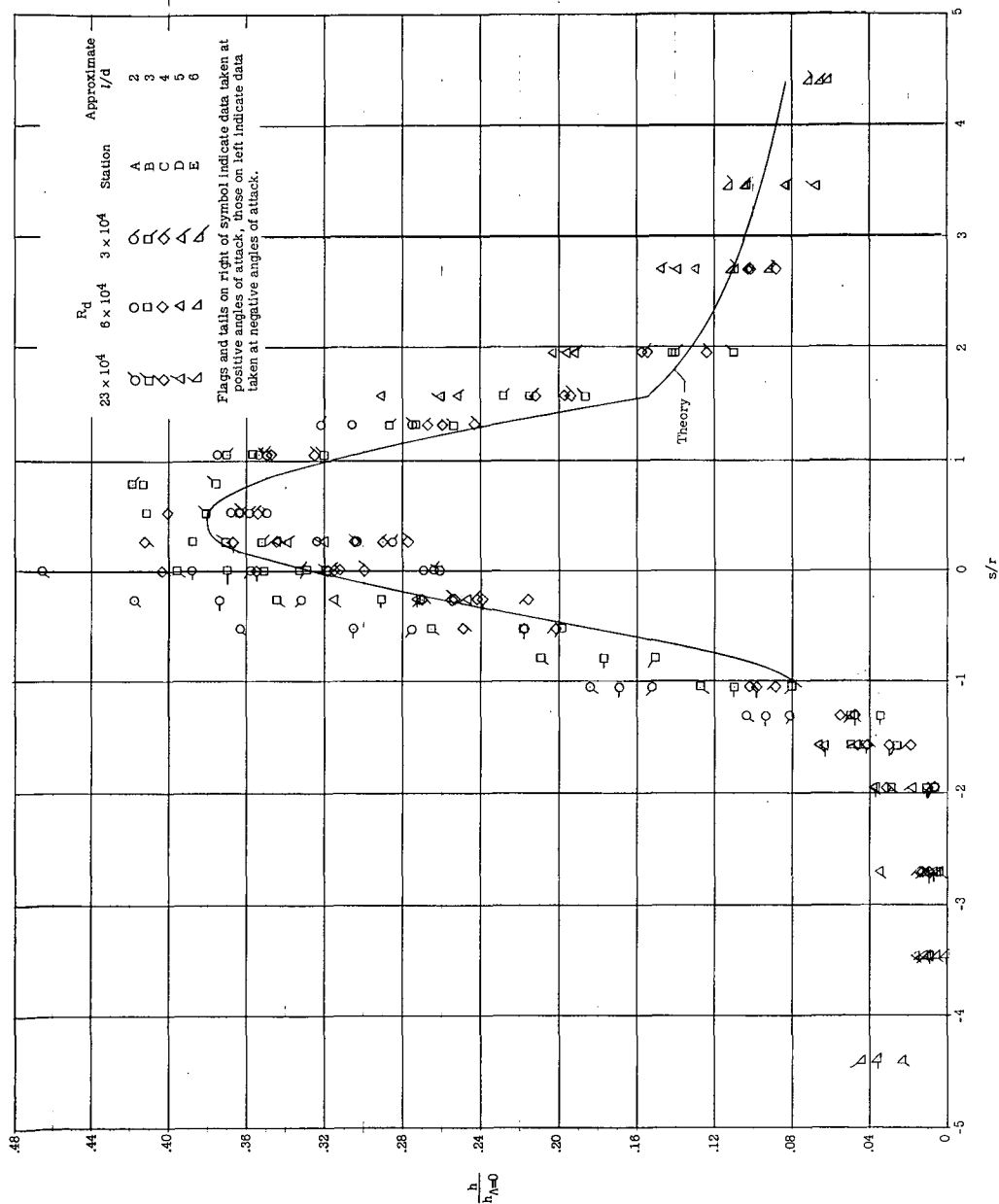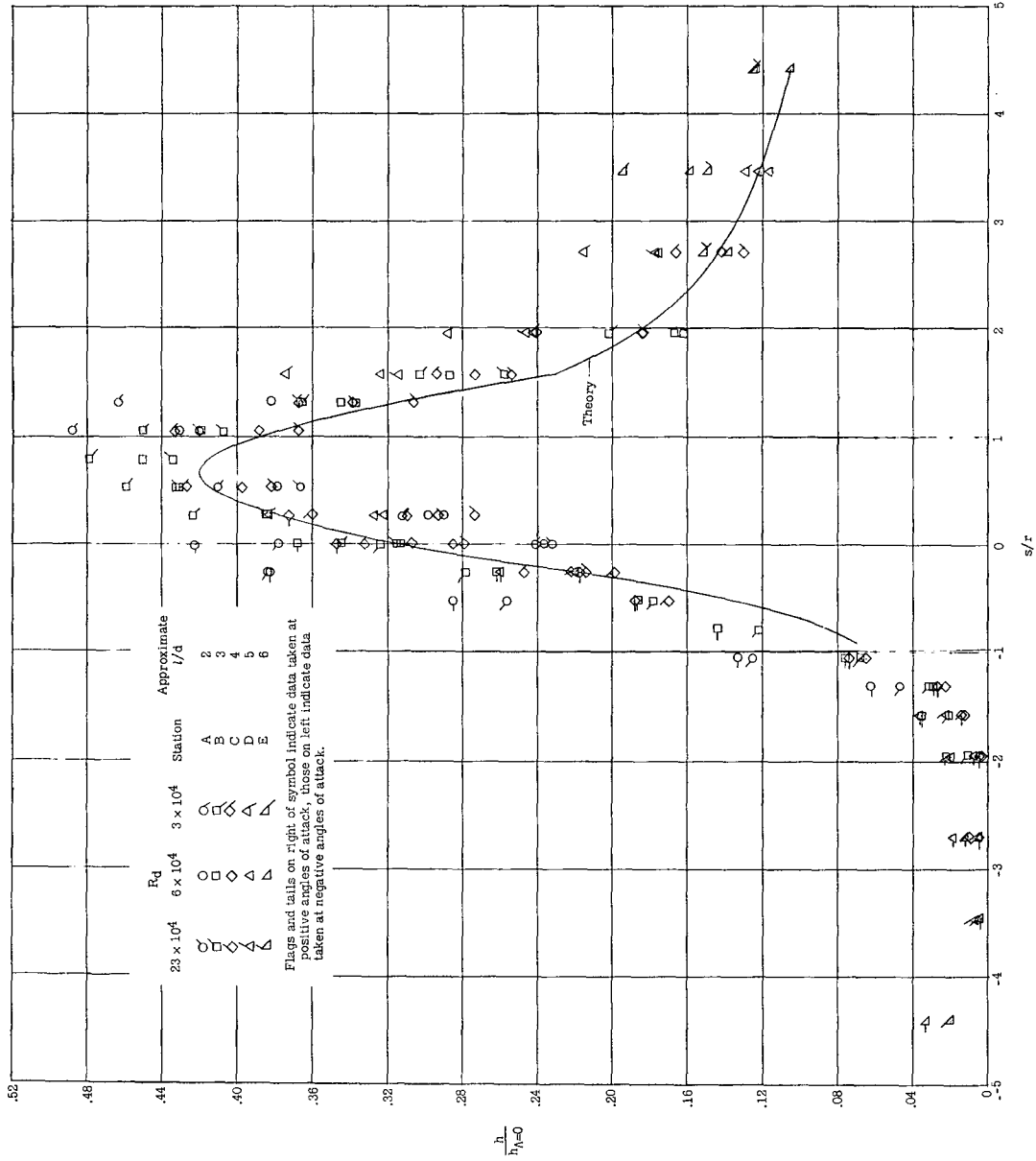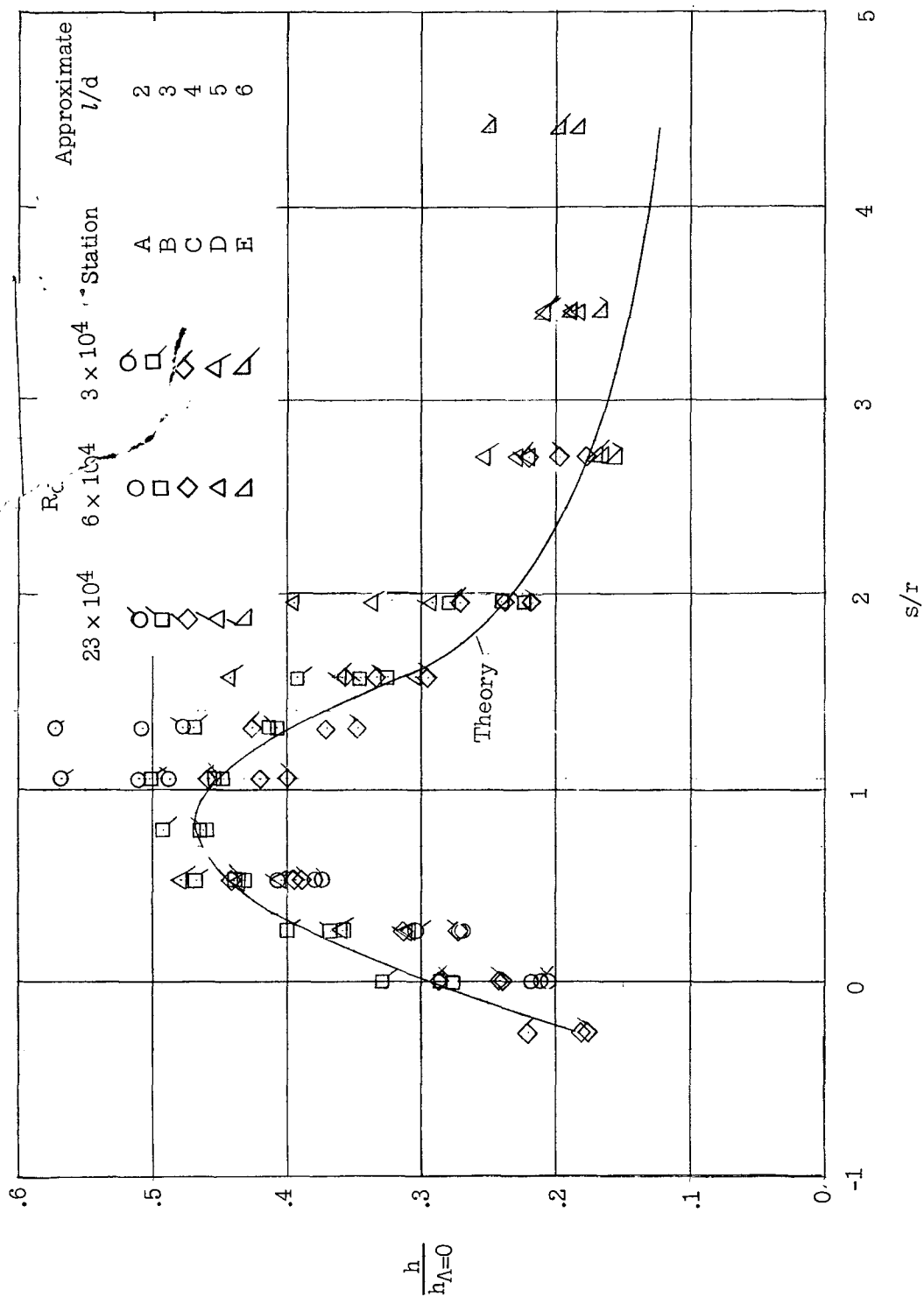
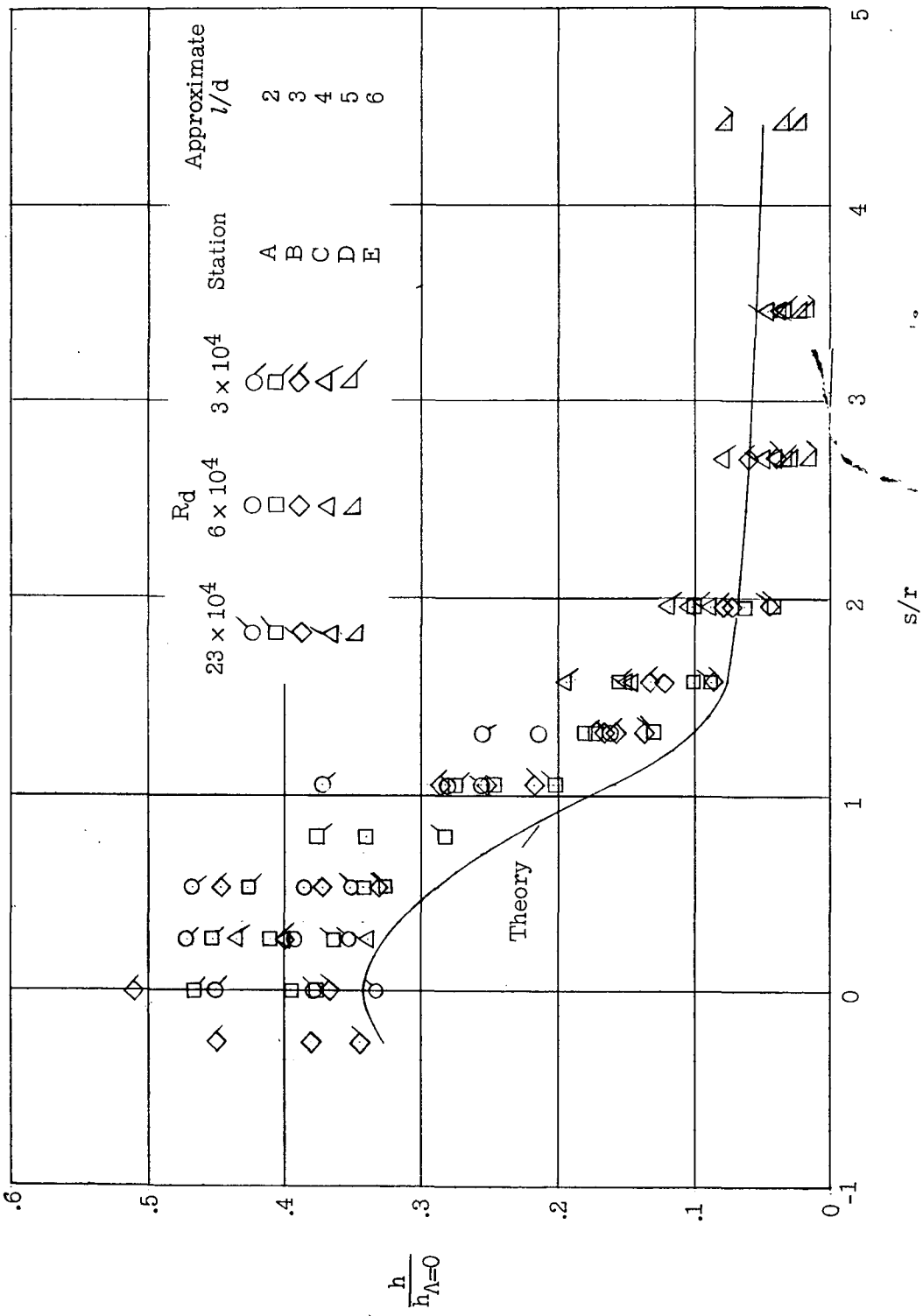(e) α = 20°.

Figure 11.- Concluded.

Figure 12.- Heat-transfer distributions of spherical-nose configuration by using swept-shock entropy. $\sigma = 0^\circ$.